



Damage modelling of carbon fibre composite crush tubes: Numerical simulation and experimental validation of drop weight impact

Drew E. Sommer^{a,*}, D. Thomson^{a,*}, O. Falcó^a, G. Quino^{a,b}, H. Cui^c, N. Petrinic^a

^a Department of Engineering Science, University of Oxford, Oxford, United Kingdom

^b Department of Aerospace Engineering, University of Bristol, Bristol, United Kingdom

^c School of Civil Aviation, Northwestern Polytechnical University, Suzhou, China

ARTICLE INFO

Keywords:

Carbon fibre
Damage mechanics
Numerical modelling
Composite laminate
High strain rate
Dynamic fracture

ABSTRACT

Angle-ply carbon fibre reinforced polymer (CFRP) crush tubes were tested in drop weight impact experiments. High-fidelity computational modelling of the dynamic impact response was performed using explicit finite element analysis in LS-DYNA. Ply-by-ply and fibre-aligned meshing was used for the composite lamina wherein the intralaminar damage was treated with a 3D rate- and pressure-dependent continuum damage mechanics (CDM) model, implemented as a user material. Delamination was modelled using cohesive tiebreak contacts to deal with the mis-matched nodes caused by the use of a structured, fibre-aligned mesh. The material aligned meshing scheme was shown to be required to capture the intralaminar splits observed in the $\pm 45^\circ$ plies. The numerical predictions showed excellent correlation with experimental measurements in terms of both the damage mechanisms and macroscopic material behaviour of the drop weight. In the simulation, interlaminar friction between delaminated plies seemed to be a main contributor of energy dissipation. Parameter sensitivity analysis showed that the interaction between the delamination fracture energy and friction can substantially influence the results and stable crushing load, in particular. For the scenario studied here, a regular structured mesh (unaligned) was shown to be insufficient for simulating realistic crack paths despite producing reasonable predictions of the force–displacement and absorbed energy.

1. Introduction

Due to their widespread use in lightweight structures and components, carbon fibre reinforced polymer (CFRP) composites are often used in applications where potential impact is a critical concern. As a result, the ability to accurately predict the material behaviour beyond the ultimate strength limits and into the fracture and damage evolution domain is crucial to the safe design of CFRP components in many industrial applications, from crash absorbing structures in the automotive industry to bird strike and hail impact resistant structures in the aeronautical industry. In recent years, much progress has been made in the constitutive modelling of CFRPs using finite element analysis (FEA) tools. However, the verification/validation of these models often relies on plate impact experiments, which, as challenging as they can be to predict, are still relatively simple test cases within the scope of typical industrial applications. Because of this, more complex loading scenarios, such as crushing or compression after impact (CAI), which tests not only the damage tolerance under impact but also the residual strength of the structure, are becoming more common for model validation.

In particular, axial crushing of composite laminates for crash worthiness applications has been extensively studied using various numerical and experimental techniques. Investigations using crush tubes [1–13] and other configurations [14–18] are prominent in the literature. Ply-by-ply modelling of composite crushing using continuum damage mechanics (CDM) and cohesive surface-based contact was performed in [19–23], however results using meso-scale (ply-by-ply) fibre-aligned meshing of composite crush tubes have to date not been reported. Simulations of composite crush tubes with $\pm 15^\circ$ off-axis plies were performed in LS-DYNA with MAT54 by Siromani et al. [24]. Reuter et al. [25] tested and analysed circular composite crush tubes with different layups. The numerical modelling, performed in LS-DYNA, employed layers of shell elements connected with tiebreak contact to simulate delamination. Recently, Grotto et al. [26] studied crushing of a cross-ply composite plate using a Discrete Ply Model (DPM). Shor and Vaziri [9] applied a local cohesive zone model, wherein cohesive interfaces are inserted adaptively between plies, for delamination and the CODAM2 (MAT219 in LS-DYNA) damage model [27–29] to

* Corresponding authors.

E-mail addresses: drew.sommer@eng.ox.ac.uk (D.E. Sommer), daniel.thomson@eng.ox.ac.uk (D. Thomson).

simulate axial crushing of a composite tube. Axial crushing of quasi-isotropic composite (IM7/8552) crush tubes was analysed by Reiner et al. [30] using three different CDM models in Abaqus/Explicit and LS-DYNA. Excellent predictions of the force–deflection and specific energy absorption (SEA) were reported, but only one shell element through the thickness was used to model the composite layup to maintain computational efficiency, so delamination was not simulated. Issues related to modelling crushing loads using a single layer of shell elements to maintain computational efficiency are discussed in [12,31]. Built-in LS-DYNA material models (e.g., MAT54, MAT58, MAT262) were applied to model composite crush scenarios in [5,12,31]. A recently developed tabulated composite plasticity and damage model has been implemented in LS-DYNA as MAT213 for analysis of composite impact [32–35]. The MAT299 composites damage model [36] in LS-DYNA includes strain rate dependence and a deformation gradient decomposition algorithm [37] and has been used to predict impact damage in composite laminates.

While previous work on the modelling of axial crushing has shown good agreement between experiments and simulations in terms of overall force–displacement, the use of heavily simplified models often relies on non-physical fitting of material parameters, and their inability to capture key energy dissipation mechanisms, such as shear non-linearity, matrix crack propagation, contact friction and fibre breakage, may leave some uncertainty with respect to their applicability/reliability in differing loading conditions. Nevertheless, such simplifications are often necessary for the evaluation of large structures in order to keep the computational cost within reason. Still, modern techniques for composite damage modelling, including state-of-the-art CDM models, fibre-aligned ply-by-ply meshing, and cohesive zone modelling (CZM) have previously been shown to accurately model composite failure [38–42].

In the present study, drop weight tests on cylindrical $\pm 45^\circ$ composite tubes have been used to evaluate the predictive capability of leading numerical constitutive models and kinematic modelling techniques in a test case where the damage and energy dissipation mechanisms play a much more significant role to the structural response of the component. The crush tubes, which had an inner chamfer of 45° on the impacted edge, were impacted along the axial direction until the impact energy was completely dissipated. The impact caused widespread matrix cracking, with angled splits oriented along the local fibre directions, and delamination damage along the length of the tube. Crushing loads can prove more challenging to model with finite elements than typical plate impact tests due to the type and extent of damage. This paper builds upon preliminary results presented in [43] and aims to accurately reproduce the experimental crushing behaviour, using physically-based models and material parameters, to test the limits of current modelling capabilities. Therefore, the results from the performed tube crush tests have been used to investigate the suitability of a three-dimensional rate-dependent constitutive model [44] and different finite element meshing strategies for high-fidelity simulations. First, a conventional meshing technique was used, which consisted of regular structured brick elements aligned with the tube axial direction using one element per ply through thickness and cohesive contact for the ply interface. However, the use of unaligned meshes, even when paired with advanced 3D damage models, has shown limited capability to describe the propagation of matrix cracks through the material, which can severely affect the accuracy of the model beyond the initial onset of damage. Therefore, a second meshing technique has also been considered, with fibre-aligned elements in each ply and cohesive contact interactions used to bond layers with non-conforming meshes. First, experimental results of the drop weight testing, including *post-mortem* computed tomography (CT) analysis of the failure mechanisms, are reported. These data are then used to validate the modelling technique described in the subsequent sections.

Several points of novelty in this paper are noted including the use of fibre-aligned, ply-by-ply meshing of non-planar composite laminates

containing off-axis plies. As mentioned above, previous studies have investigated the use of fibre aligned meshing for plate impact test cases. However, axial crushing puts greater demands on the predicted fracture mechanisms, the residual strength and stiffness of the damaged material, and other aspects such as the friction between cracked interfaces and between specimen and impactor. The solution in this case showed sensitive to many of these aspects that may be less relevant in out-of plane impact loading, and for which the present study may serve as more thorough validation.

Furthermore, the experimental validation of the numerical modelling framework (including state-of-the-art composites CDM model and kinematic meshing) demonstrated successful reproduction of, not only the energy absorption and force–displacement curves, but also the composite damage mechanisms, which has received little attention in the literature for the case of angle-ply crush tubes. In addition, the influence of the meshing strategy (material-aligned vs regular, structured) was also shown and highlights the importance of a robust kinematic meshing procedure in addition to the material constitutive model. The parameter sensitivity in the proposed analysis of crushing applications has not previously been reported including the effects of strain-rate, and the constitutive model was validated for composite crushing without excessive parameter calibration using a fibre-aligned mesh for the first time. Finally, the modelling strategy was validated for two different trigger geometries to investigate the effect of subtle differences on the damage evolution.

2. Experimental work

2.1. Tube manufacturing and test specimen configuration

The composite crush tubes were fabricated from unidirectional (UD) Hexcel IM7/8552 prepreg by wrapping plies on a filament winding core. The stacking sequence was $[+45_4/-45_4]_{2s}$, where the ply orientations are given with respect to the tube axis direction. The nominal cured ply thickness was 0.125 mm. All tubes were manufactured with a length of 100 mm, inner diameter of 40 mm, and outer diameter of 48 mm as shown in Fig. 1. Debulking was performed after every eight plies to reduce trapped air and voids. After all plies were deposited, the winding core was vacuum bagged before the part was cured in an autoclave following the manufacturer recommended cure cycle. The specimen quality was checked by CT scanning the tube after curing and no concerning issues were found. After inspection, the tubes were cut to the specified length using a water-cooled diamond disk saw by trimming the excess length and a 45° chamfer was machined on the impacted end of the tubes, as shown in Fig. 1. Four replicates ($n = 4$) were tested for each chamfer geometry (inner and outer).

2.2. Experimental setup and data reduction

A drop weight test rig, shown in Fig. 1, was used to perform the impact experiments. The steel impactor had a mass of 10.0 kg and was dropped from an initial height of approximately 5.1 m. This produced an impact velocity of around 10.0 m/s and an impact energy of approximately 500 J. A laser extensometer was used to verify the drop height before each test and a Photron high-speed camera was used to record the failure process at frame rates up to 75,000 fps with a field of view of up to 384×584 pixels at a 4.5 pixels/mm resolution. The displacement of the impactor, painted with a black on white speckle pattern, was measured via 2D digital image correlation (DIC). The DIC data reduction was performed with the software GOM ARAMIS using a subset size of 19 pixels.

To fix the base of the tube in place during the impact event, the specimens were fitted onto a steel support with a 40 mm diameter insert, as seen in Fig. 1, before releasing the drop weight. The displacement history of the impactor, calculated using DIC, was differentiated successively to obtain the velocity and acceleration histories, from which the initial impact velocity was verified and the impact force, F , was approximated ($F = m \times a$).

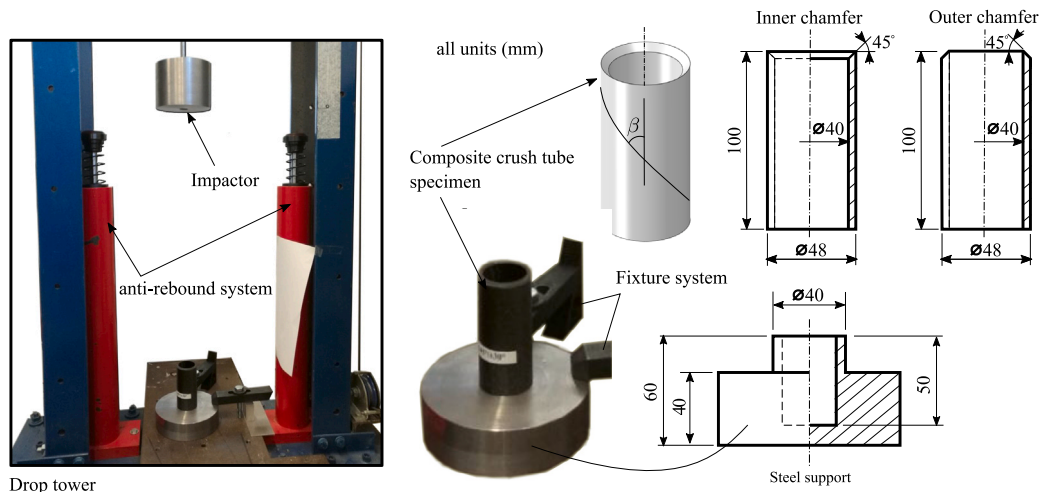


Fig. 1. Crush tube geometry and experimental drop weight setup.

Table 1

Measured peak force (onset) and maximum drop weight displacements of the four replicates for both inner and outer chamfer geometries.

Inner chamfer		
	Peak force (onset) [kN]	Max. Disp. [mm]
Exp. #1	72.1	13.6
Exp. #2	40.5	21.5
Exp. #3	59.5	20.8
Exp. #4	66.4	17.7
Avg.	59.6	18.4
Outer chamfer		
	Peak force (onset) [kN]	Max. Disp. [mm]
Exp. #5	56.2	18.5
Exp. #6	63.4	20.9
Exp. #7	71.7	20.9
Exp. #8	66.7	19.1
Avg.	64.5	19.8

2.3. Experimental results

The peak forces, measured during the damage initiation phase, and maximum crushing displacements for each replicate of the current experimental campaign are reported in Table 1 for both chamfer geometries.

2.3.1. Inner chamfer

The obtained displacement histories, velocity histories, and load versus displacement for the four repetitions are shown in Figs. 2 and 3, respectively. For the displacement evolution, Fig. 2(a) shows the raw data obtained from the DIC analysis and shifted to start at the first point of contact between the tube and the drop weight. However, because of the differentiation process, the force data was excessively noisy when using the raw displacement data. Therefore, for illustrative purposes, the displacement data was sampled at a lower frequency for the force and velocity calculations (20,000 for specimens N1, N2, and N3, which were originally recorded at 40,000 fps, and 25,000 for N4, which was recorded at 75,000 fps).

The four tests showed some variability, possibly due to minor differences in manufacturing quality and axial specimen alignment with the impactor. Other than the variability in the total displacement, the force–displacement curves for each repetition showed similar behaviour, with an initial gradual increase in force reaching a peak at approximately 4.0 mm displacement, which corresponds to the depth of the chamfer. After this point, a significant drop-off can be observed in the crushing force, followed by a damage evolution stage until the drop

weight is slowed to a stop. Therefore, the region up to the peak force can be considered as the damage initiation phase, while the remainder of the test can be considered a damage propagation phase.

Ignoring the high-frequency oscillations in the force–displacement curves, after the initial drop-off, the average force during the crack propagation stage was calculated to be approximately 50% of the initial peak force. The effect of this change in behaviour can also be seen in the velocity history, which shows a subtle change in slope after approximately 0.5 ms for all four tests. Finally, the lower frequency oscillations in the propagation region may be an indication of stick-slip behaviour in the crack opening process, which was also observed for some of the surface cracks in the high-speed images.

While slight compliance in the setup was noted immediately following the onset of contact between the drop weight and specimen, wherein minute vertical translation of the specimen is seen while it fully settles into the base support, this should not influence the measured results beyond the first few instants of the test, before even the first signs of damage. In addition, the experimental force–displacement curves obtained in the present work are qualitatively similar to results in [25] for a [(45/−45)₅/45]_s layup with a slightly different diameter and thickness, but nearly identical cross-sectional area. The fact that the crushing displacement was much lower in the present study can be attributed to the lower impact energy, which required a shorter crushing length to fully dissipate.

2.3.2. Outer chamfer

The measured drop weight displacement and velocity histories for the outer chamfer are shown in Fig. 2(c), (d) while Fig. 3(b) shows the force–displacement and total crushing displacement. Good repeatability was observed with the outer chamfer. The displacement and velocity histories exhibit similarities to Exp. #2 and #3 with the inner chamfer. Longitudinal ply splits propagating along the fibre direction were present in the outer chamfer tests similar to those seen with the inner chamfer (described in Section 2.4).

2.4. Post-mortem analysis

After testing, the crush tube from Exp. #4 (inner chamfer), whose behaviour was closest to the average of all four tests, was CT scanned to obtain a high-resolution, 3D reconstruction of the fractured composite structure. The specimens were scanned in a high-resolution CT system V|tomex|L 450 (GE Phoenix X-ray) with an incorporated 300 kV microfocus and a 450 kV macrofocus X-ray tube. The scan resolution was 30 μm. High-resolution CT scanning has been used previously to analyse damage in laminated composites [45]. The CT scan permitted

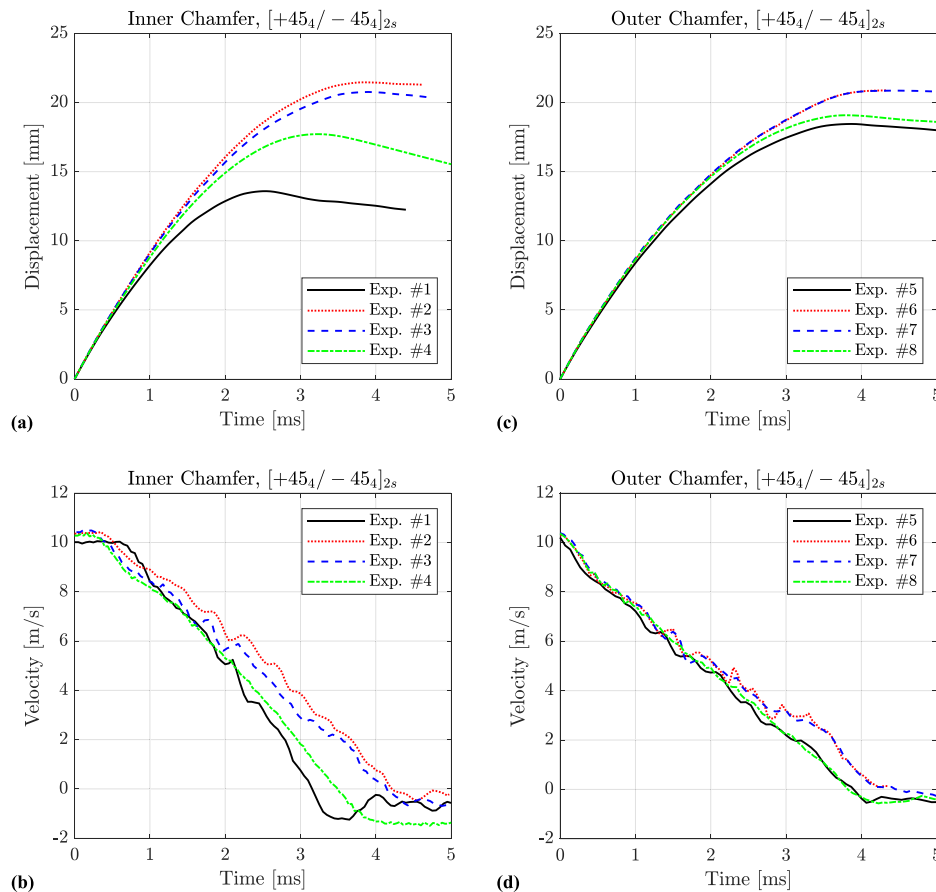


Fig. 2. Experimentally measured drop weight (a) inner chamfer displacement, (b) inner chamfer velocity, (c) outer chamfer displacement, and (d) outer chamfer velocity histories.

qualitative analysis of the fracture mechanisms and quantitative measurement of the crack density and crack length for comparison with numerical predictions.

In general, the failure mode of the tubes might be considered as a combination of splaying and fragmentation modes frequently discussed in the literature [2]. Experiments performed by Siromani et al. [24] on crush tubes containing 0° , 15° and -15° plies displayed longitudinal ply split in the outer layers of angled plies similar to those seen in the present study (see Fig. 4). The damage appears qualitatively different from results reported in [25], but the referenced failure is reported after much greater crushing displacement than in this work. Additionally, the stacking sequence used here contains large ply blocks, which can be considered as increasing the apparent lamina thickness, while dispersed plies are used in [25]. Similar angled ply splits were observed by Liu et al. [46] for $\pm 45^\circ$ cylindrical carbon/epoxy crush tubes.

In the present work, the failed tubes exhibited significant matrix cracking parallel to the fibre directions at $\pm 45^\circ$ and interlaminar delamination, but limited fragmentation of the carbon fibres, with the split plies bending out of the way instead. The delaminations can be distinguished in two categories, first, delamination between layers with the same fibre orientation, and second, delamination at the interface of different fibre orientations. Fig. 4 shows two cut planes in the *post-mortem* CT scan. In the vertical cut plane, shown in Fig. 4(a), delaminations between ply blocks and within a ply block are observed. These delaminations are combined with other failure mechanisms such as fibre bridging mainly related with external ply blocks. Delaminations within ply blocks appear primarily on the interior of the tube. The lengths of these delaminations seem to be shorter than the delaminations between ply blocks. The outer three groups of clustered plies seem to maintain the integrity of their laminated structure, while the delaminations occur mostly in between them. This is particularly

evident from the horizontal ($r - \theta$ plane) view cut. The intralaminar damage in these plies seems to be primarily matrix failure with cracks oriented along the fibre directions. However, some delamination within the outer layers of blocked plies is observed in Fig. 4(b). In addition, the vertical cut in Fig. 4 shows the influence of the chamfered edge on the damage evolution within the tube, as most plies appear to be pushed outwards with only the two innermost ply blocks bending in towards the centre of the tube.

Aside from the more qualitative analysis above, the high-resolution CT scan also allowed for some quantitative measurements of the approximate number of intralaminar cracks, crack lengths and delamination areas. The number and length of the matrix cracks on the outer ply block were measured by fitting three-dimensional splines along the crack path. However, for the interior plies, while a significant increase in crack density could be observed, this was not easily quantifiable.

3. Numerical modelling

The progressive damage and failure analysis of the drop weight impact of the composite crush tube was performed in LS-DYNA. A ply-by-ply model with a semi-automated fibre-aligned mesh generator was developed. The intralaminar damage behaviour of a UD ply was modelled using CDM, while a CZM was used for the interlaminar response. Fully damaged elements are removed from the simulation to simulate crack-band formation, improve the numerical behaviour and avoid highly distorted elements during the crushing analysis. Eroding contact was applied between the drop weight and CFRP and the cohesive zone model was enforced using tiebreak contact. Frictional contact between the drop weight and CFRP and delaminated plies was included. Typical static friction coefficients for contacts between CFRP–steel reported in the literature range from 0.2 to 0.7 [19,47–49], with the dynamic

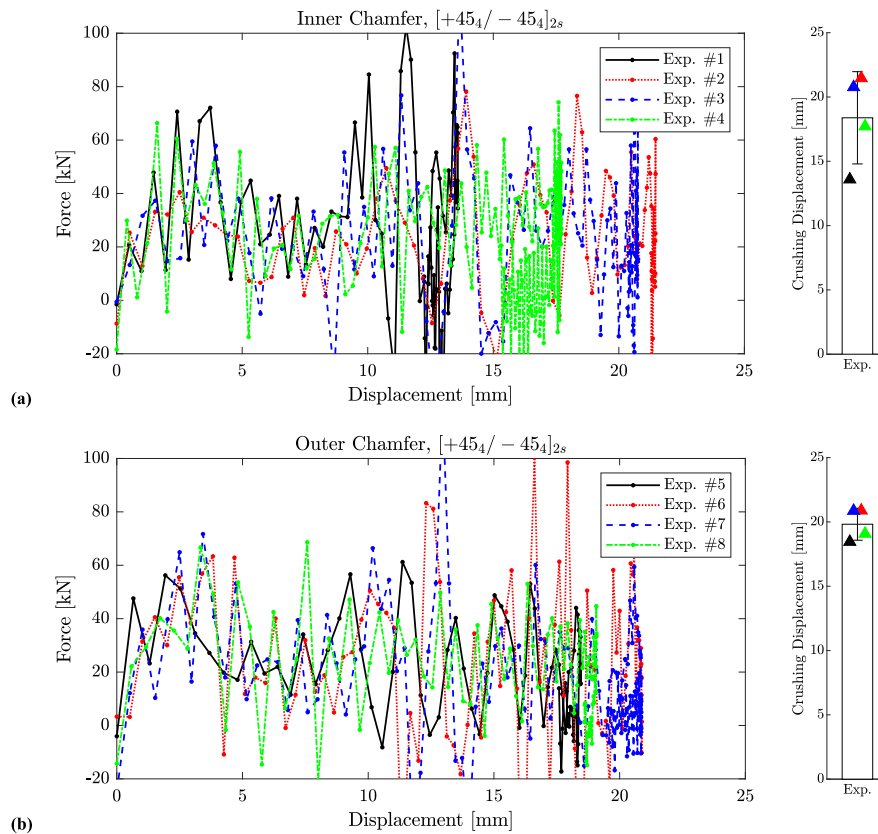


Fig. 3. Measured force–displacement curves from (a) four experimental replicates with an inner chamfer and the total crushing displacements (avg.: 18.4 mm, CV: 19.5%) and (b) four experimental replicates with an outer chamfer and the total crushing displacements (avg.: 19.8 mm, CV: 6.3%).

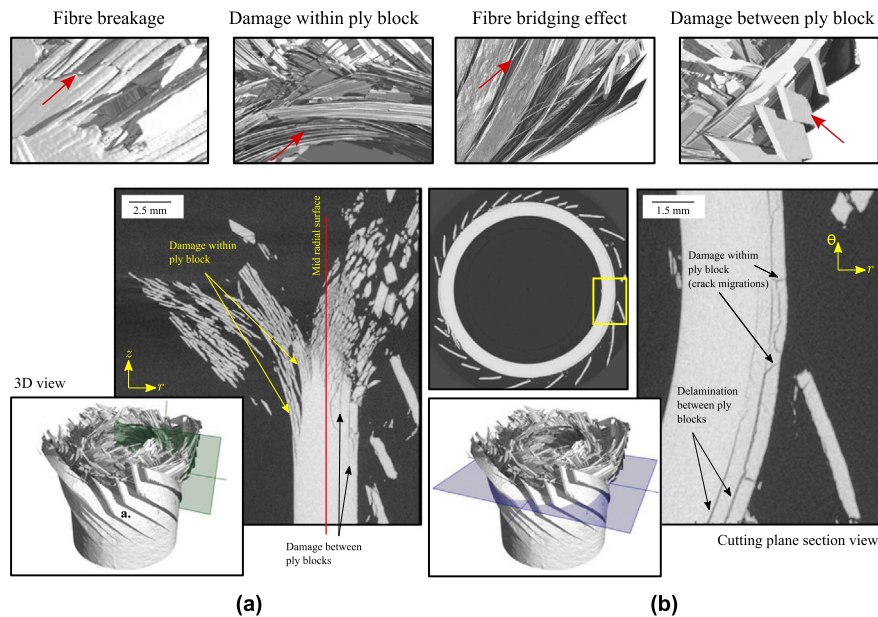


Fig. 4. (a) Vertical and (b) horizontal cut planes from a *post-mortem* CT scan showing different damage mechanisms.

friction coefficient typically 30%–40% lower [36,48,50]. In this work, static and dynamic friction coefficients between the impactor and CFRP of 0.5 and 0.3, respectively, which are in line with the reported values, were found to give good results. To the best knowledge of the authors, such a modelling strategy with fibre-aligned mesh deployed in this work has not been previously applied to a composite crush tube. The numerical model was validated by comparing fracture mechanisms and

drop weight response measured in the experimental section. The model setup is illustrated in Fig. 5.

3.1. Constitutive modelling

The UD ply behaviour was modelled by a pressure- and rate-dependent plasticity and damage model, implemented in LS-DYNA as

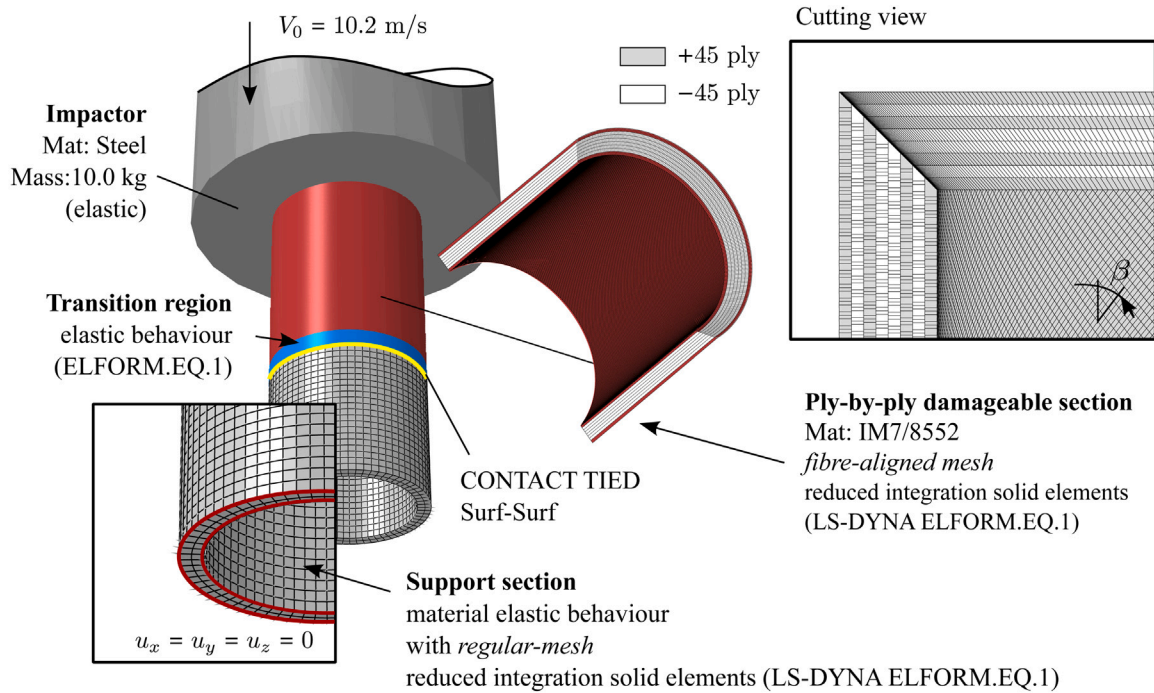


Fig. 5. Numerical model of the drop weight assembly and detail view of the fibre-aligned mesh.

a user material model (UMAT) [44]. In the previous work in [44], the model was extensively calibrated using quasi-static (QS) and high-rate (HR) experimental data from [51–53]. The CZM is enforced using native LS-DYNA tiebreak contacts. A contact based formulation is favoured over cohesive elements in the absence of coincident nodes at the ply interfaces caused by the fibre-aligned mesh. The intra- and interlaminar models are briefly summarised in the following sections, and a more detailed description can be found in Appendix A.

3.1.1. Intralaminar behaviour

The constitutive model, reported in [44], thoroughly describes the behaviour of the UD CFRP within a ply as the result of different fibre and matrix-dominated mechanisms. The underlying elastic response is assumed to be transversely isotropic, with the longitudinal modulus dominated by the high-stiffness reinforcing fibres, while the transverse and shear moduli are dominated by the polymeric matrix and incorporate the characteristic strain-rate dependent behaviour typical of epoxy resins.

Beyond the elastic response, the model incorporates energy dissipation through plastic deformation in the matrix and through different failure mechanisms, which can be in the form of either fibre tension, fibre compression, or matrix cracking.

The three-dimensional plasticity law aims to describe the effects of progressive micro-scale damage and matrix plasticity as the accumulation plastic strains along a critical localisation plane parallel to the fibre direction. The critical localisation plane is determined by the angle, θ_{lp} , that minimises the following strain-rate and pressure dependent yield function:

$$f = \bar{\sigma} [\sigma, \theta_{lp}] - \tau_y [\dot{\epsilon}_p] = \alpha \sigma_n + \sqrt{\tau_{n1}^2 + e \tau_{m1}^2} - \tau_y [\dot{\epsilon}_p] \quad (1)$$

Where $\bar{\sigma} [\sigma, \theta_{lp}]$ is the effective stress computed from normal and shear traction components, σ_n , τ_{n1} , and τ_{m1} , acting on the localisation plane, θ_{lp} , and $\tau_y [\dot{\epsilon}_p]$ is the rate-dependent yield stress. The model parameters α and e define shape of the yield envelope and the pressure-effect.

Together with the above yield condition, the description of the non-linear plastic behaviour is completed with a double-voce strain

Table 2

Material properties of UD IM7/8552. Source: Adopted from [44,56,57].

Property	Value		Property	Value	
E_{11}	162.1	GPa	Y_T	60.2	MPa
E_{11c}	140.9	GPa	Y_C	250	MPa
E_{22}	9.7	GPa	$S_{12}(= R_{n1})$	112.7	MPa
G_{12}	4.7	GPa	$S_{12}(= R_{n1})$	112.7	MPa
ν_{12}	0.362	–	p_e	0.2	–
A	60	MPa	p_c	0.2	–
B_1	33	MPa	X_T	2625	MPa
C_1	130	–	X_C	1451	MPa
B_2	25	MPa	G_{IC}	0.2	N/mm
C_2	10	–	G_{IIC}	0.9	N/mm
α	0.1	–	G_{IC}^+	82.0	N/mm
e	0.9	–	G_{IC}^-	101.6	N/mm
r_y	1E–3	s			

hardening law and non-associative plastic flow, described in more detail in [44].

In parallel, three independent stress-based failure criteria are considered, one for each of the main failure mechanisms. Matrix cracking is assumed to occur on the same localisation plane as the plastic deformation once the effective stress reaches either the rate-dependent shear strength or once the normal traction, σ_n , reaches the rate-dependent transverse tensile strength. In the case of fibre failure, tensile failure is predicted by a maximum stress criterion, and for fibre compression, a kinking failure criterion [54,55] is used.

Finally, damage evolution is described in the continuum damage mechanics framework through a smeared crack formulation, which releases the fracture energy associated to the relevant failure mechanism over the full length of the crack within a solid element through the linear softening of the associated matrix- or fibre-dominated stiffness properties.

Material parameters for a homogenised UD ply were adopted from [44,56], where the same model was calibrated for the IM7/8552 material used in this study. The material properties are reported in Table 2.

3.1.2. Interlaminar behaviour

Delamination was modelled using a cohesive zone contact natively available in LS-DYNA. Tiebreak contact Option 7 (Dycoss Discrete Crack Model) [58] was used for pressure dependent delamination failure initiation, given by Eq. (2), where σ_n is the normal stress, σ_s is the shear stress, NFLS is the failure stress in the normal direction, SFLS is the shear failure stress, and PARAM is the friction angle. With this initiation criteria, the strength of the interface is increased by pressure following the same logic used in the intralaminar constitutive model. In this work the tiebreak contact formulation is combined with the effect of friction as an additional energy dissipation mechanism. The interlaminar friction properties between delaminated plies were adopted from [36].

$$\left[\frac{\langle \sigma_n \rangle}{\text{NFLS}} \right]^2 + \left[\frac{\sigma_s}{\text{SFLS} - \sin(\text{PARAM}) \min(0, \sigma_n)} \right]^2 = 1 \quad (2)$$

The interfacial strengths were elevated to account for strain-rate effects while using a rate-independent interface model by using the dynamic values from Table 2 assuming $\text{NFLS} = Y_T$, $\text{SFLS} = S_{12}$ and $\text{PARAM} = 12^\circ$, to match the frictional effect on the intralaminar strength properties, $p_c = 0.2$ [52]. The mode I and mode II fracture energies were assumed to be $G_{IC} = 0.25 \text{ N/mm}$ and $G_{IIC} = 1.0 \text{ N/mm}$, which are in line with values reported in the literature [56,59].

3.2. Meshing technique and element erosion

To accurately model the failure mechanisms observed in the experiments, a fibre-aligned meshing technique was selected. This aligned meshing strategy has been shown to accurately reproduce the fracture mechanisms in UD fibre-reinforced composite laminates and has gained attention in recent years [38–42,60,61]. By orienting mesh lines along the local, orthotropic material axes, the crack propagation can be more realistically captured. In general, the mismatching mesh at the ply interface lends to the use of contact based cohesive modelling, which is employed in the present analysis. Mesh regularisation [62] was used to reduce mesh sensitivity. Other issues specifically associated with mesh sensitivity in crushing applications have been studied [16,31], and, in this work, a fibre-aligned mesh yielded excellent behaviour.

The crush tube mesh was divided into three regions (see Fig. 5) to improve the computational efficiency of the model. First, a refined, fibre-aligned mesh was used under the impactor. This region extended 50 mm along the length of the tube before reaching a short transition region. On the impacted end of the tube, the nodes are adjusted to conform to the chamfer geometry as seen in the top right view cut in Fig. 5. Then, a transition region was used to connect to a coarse, regular mesh (support region), used away from the damage zone to reduce the number of elements. The transition and support regions were modelled as elastic and were connected using tied contacts, and the support region was meshed with $1 \text{ mm} \times 1 \text{ mm}$ elements with two elements through the thickness of the laminate. Smeared composite properties are applied. Reduced integration solid elements (ELFORM.EQ.1 in LS-DYNA) with hourglass controls (HG=4) are used throughout. The models contained approximately 750×10^3 elements and were run on a Linux workstation using MPP LS-DYNA R11 on 30 CPU cores. The run time was approximately 94 h to reach 4 ms of simulation time.

The elements in the fibre-aligned mesh were $0.4 \text{ mm} \times 0.2 \text{ mm}$ (longitudinal \times transverse). This element size and aspect ratio was chosen as the best trade-off between efficiency and accuracy. The upper bound of the element dimensions is determined by the energy dissipation requirements [40]. Further evaluation of the mesh sensitivity is discussed in Appendix B. Increasing the element aspect ratio beyond 2:1 seemed to be less reliable for handling the crushing mechanics observed in the studied configuration. Since the layup used blocked/clustered plies, eight layers of elements were used through the thickness, which corresponds to one element per orientation ply block, such that each

element represents four plies of UD tape oriented at either $+45^\circ$ or -45° degrees. This assumption was useful for reducing the model size and is typical for ply-by-ply meshing of composite laminates. While this assumption appeared to be appropriate for the outer ply-blocks, the post-mortem CT scans showed delamination between layers within a ply block on the interior of the tube. To account for delamination within a ply-block, the interlaminar fracture energies were increased by a factor of four to match the number of delamination interfaces observed in the experiments. All of the numerical results shown in the following sections use increased delamination fracture energy unless otherwise noted. This decision to adjust this model parameter was physically based on the experimental observations and the availability of computing resources which limited the model size to eight layers. Meanwhile, all other properties are adopted from the literature for a single, UD ply or interface between plies. Finally, element erosion was used to remove failed elements from the analysis and avoid excessive element distortion issues. In the present analysis, element erosion is triggered by complete failure (i.e., damage variable equals unity). However, for matrix damage, compression on the fracture plane prevents failure and the material should conserve its stiffness in the normal direction (as per IFF model described previously). Additional geometric failure criteria are included to remove severely distorted elements that may not have been eroded following the previous criteria. Deletion of failed elements also simulates the formation and propagation of a crack. However, in the case of crushing experiments, erosion of failed elements (while necessary for stability) may prevent the formation of the debris wedge that is often observed in the literature and helps to drive delamination damage. Despite the challenges associated with element erosion, it is a widely used technique for crack modelling and was effectively employed in the present analysis in combination with the fibre-aligned meshing strategy.

The fibre-aligned mesh in the first region was generated automatically using scripting functions. This was performed by meshing a rectangular parallelogram tilted with an angle matching the fibre orientation angle. The length is equal to the length of the damageable region and the width of the horizontal side is the local circumference of tube measured with the radius of the ply that is being meshed. The input element dimensions are then slightly adjusted to ensure that the mesh is periodic and coincident nodes are located on opposite edges of the meshed domain. Then, a geometric transformation is performed to “wrap” the mesh and create a cylinder. The coincident nodes are merged to join the mesh into a closed, cylindrical section. In this way, the circumferential uniformity of the mesh is ensured.

4. Results and discussion

Results from the numerical simulations are presented in the following sections and compared with experimental measurements where applicable. Both the inner and outer chamfer trigger geometries were analysed and results for both cases are included herein. Since the CT scanning was limited to the inner chamfer, the focus in the following sections will be on this geometry. All results shown below are for the inner chamfer unless stated otherwise.

4.1. Inner chamfer

4.1.1. Macroscopic failure predictions

The tube crush analysis is depicted in Fig. 6(a), where the evolution of the crushing/damage is shown over four frames. Cracks nucleate in the outer ply, which is the first to come in contact with the impactor. Matrix cracks propagate along the local fibre-direction of each lamina. The fibre-aligned mesh promotes accurate modelling of this cracking behaviour. The splits continue to grow and the angled plies “unwind” around the tube. These strips bend and experience frictional contact with the drop weight (hidden in this figure to improve visualisation of the CFRP). Delaminations grow as the drop weight continues to crush

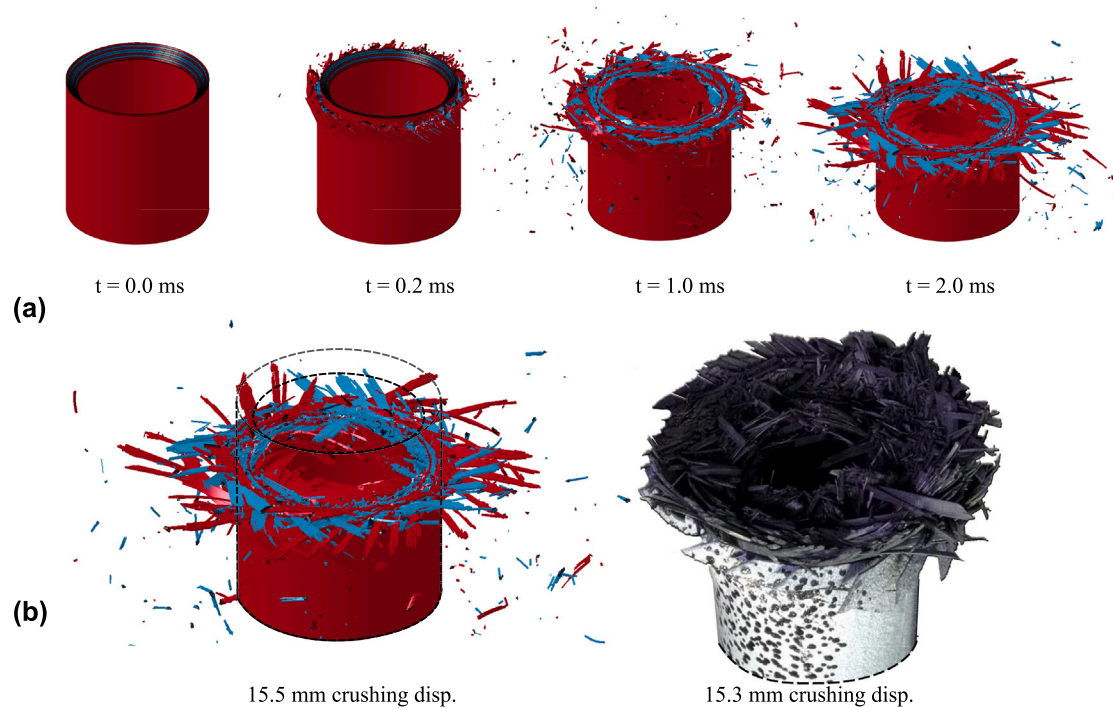


Fig. 6. (a) Simulated evolution of the tube crushing. (b) Qualitative comparison between the analysis and experiment of the failed crush tube after the impactor rebound.

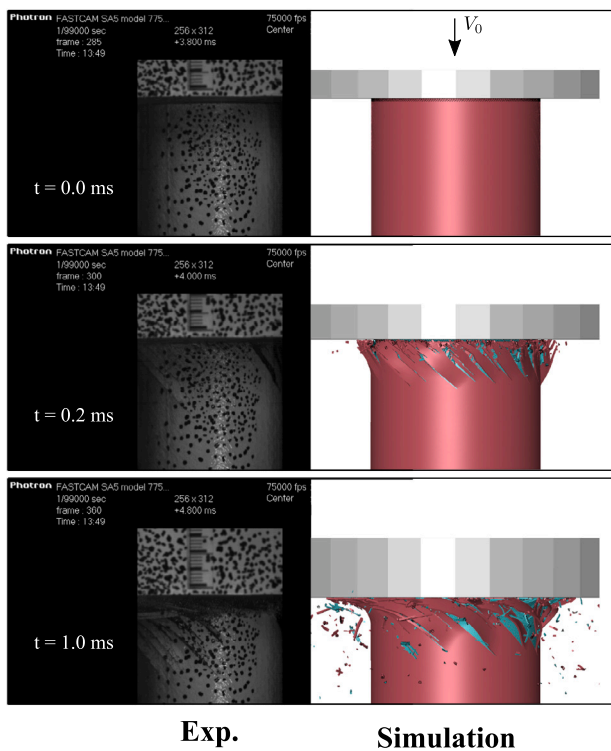


Fig. 7. Side view of the drop weight impact: experiment (left) vs simulation (right).

the specimen. The outer ply seems to delaminate the furthest as the splits propagate and the ply "unwinds". Fig. 6(b) shows the analysis next to a tested crush tube. The macroscopic damage predictions show good qualitative agreement with the experimental observations.

A side view of the drop weight impact is shown in Fig. 7. The 45° cracks seen in the experiment are reproduced by the numerical

simulation. At $t = 1$ ms, the model seems to slightly under-predict the crack length, but the overall crack morphology is in good agreement with experimental observations.

The matrix cracks in each ply are shown in Fig. 8 by displaying the deleted elements in the undeformed configuration. Each layer of elements represents four plies of UD tape oriented at either +45° or -45°. The angled splits along the local fibre directions are clearly seen, particularly in layers seven and eight. After 3.9 ms, the damage in the interior layers seems to propagate approximately equal distances along the length of the tube, while the propagation distance appears to increase in the outer two ply blocks. Widespread damage and element erosion is observed in the embedded plies.

The prediction of the delamination of the interfaces was also investigated. Fig. 9 shows a side view of the delamination damage (red) at the interface between the outer two plies (layers 7 and 8). The approximate delamination area was computed for each interface and reported in Fig. 9. The delamination propagated furthest at the outermost interface and the delamination area seemed to reduce at each interface moving towards the mid-plane of the tube. The inner most interface between plies 1 and 2 showed a slight increase compared to the adjacent interfaces, but less delamination was predicted in the interior interfaces compared to those towards the exterior. The disbonding between outer layers appeared to initiate in the early stages of the impact as a result of the chamfer. Further, the chamfer has a slight impact on the delamination areas because the ply length increases slightly along the radius. At the ply 7 – ply 8 interface, strips of split plies can delaminate further, locally, along the fibre-direction.

Finally, while a quantitative measure of the plastic strain energy was not possible from either the models or the experiments, significant permanent deformation can be observed in the tube at the end of the experiment, Fig. 6(b). Fig. 10 highlights the extent of plastic deformation predicted in the remaining un-failed elements for the baseline model (4× delam. energy, contact friction, aligned mesh), which qualitatively matches the final deformed shape of the test specimen.

4.1.2. Comparison of predicted fracture mechanisms and experimental observations

Overall, the predicted fracture morphology qualitatively appears to reproduce the damage seen in the physical tests. Fig. 11 compares

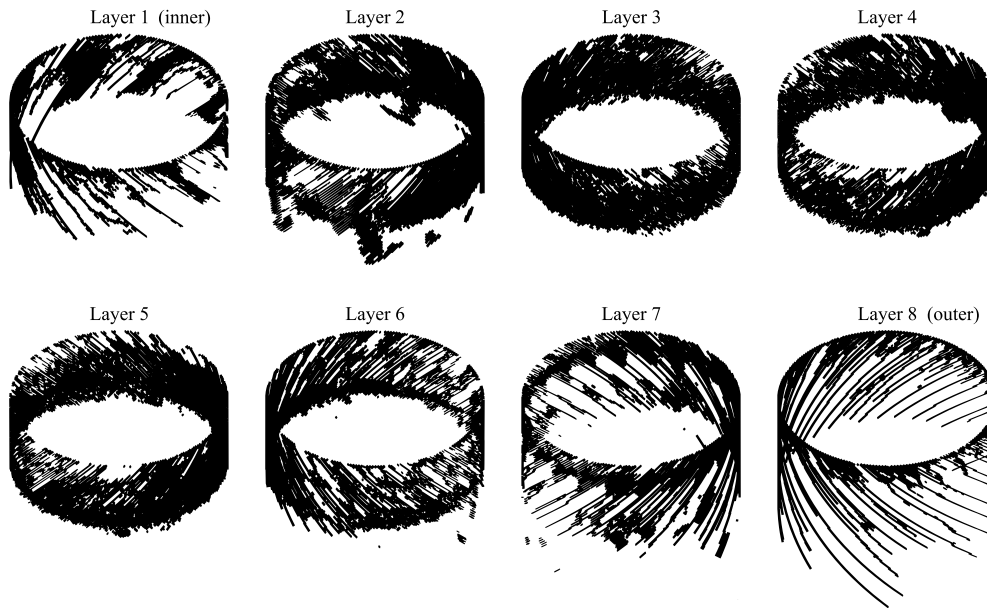


Fig. 8. Deleted elements (representing damage) at $t = 3.9$ ms in each ply of the analysis shown in the undeformed configuration.

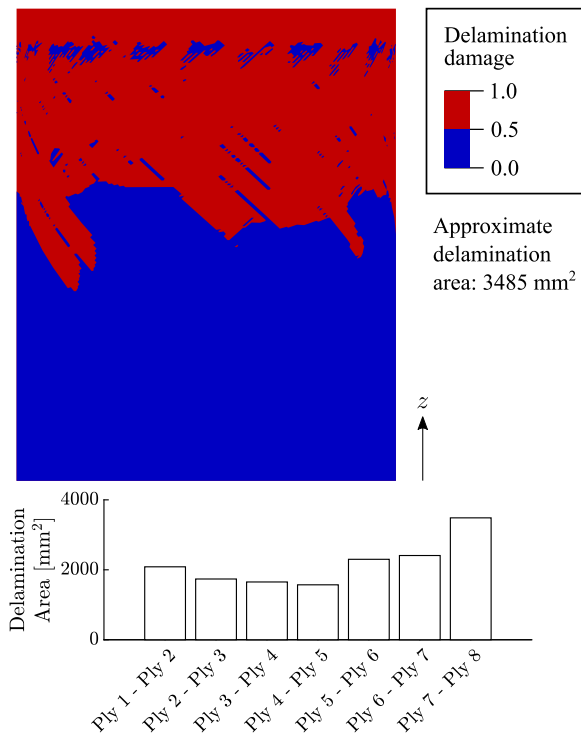


Fig. 9. Side view of the cohesive zone model (delamination) damage between layer 7 (-45°) and layer 8 ($+45^\circ$) and approximate delamination areas at each interface.

cross sections from the CT scan to those from the analysis. The large delaminations and cracks parallel to the fibre directions are captured by the simulation. Furthermore, delamination and intralaminar cracks are seen in plies 6 and 7 in both the CT scan and the analysis. At the location of this cut plane, little to no damage is seen in the inner 4 ply blocks or so. Additionally, we note that the delaminations here primarily occur at the interface between ply blocks. The intralaminar damage comes mainly in the form of transverse matrix cracks. However, the CT scan does reveal some interlaminar cracks between the -45° plies within the ply block in layer seven. Finally, the regular mesh, shown

in Fig. 11b, produces sequential element erosion at the crash front and does not accurately capture the failure mechanisms observed in the experiment.

Fig. 12 shows the analysis of the crack length and crack density estimates, which were used as quantitative metrics to compare the prediction with the experiment. The cracks in the outer surface are the focus of this analysis since they are the most clearly seen, even in the *post-mortem* CT reconstruction. An estimate of the crack density is taken by counting the number of (macroscopic) splits around the circumference of the tube. Some judgement is required when deciding which cracks should be included in this measurement. For layer 8, the number of cracks seen in the experiment ranged from 31–40 cracks in ply 8, while the analysis produced 34 cracks in the same layer. Both the simulation and the experiment showed the longitudinal splits along the local fibre direction in the outer layers.

Next, the crack lengths measured in the CT scan, by creating a spline along each visible crack to compute the length, as shown in Fig. 12, are compared to the simulation predictions. The predicted crack lengths were measured in the same way. The sample sizes were $n = 16$ (exp.) and $n = 34$ (sim.). The average crack length predictions are in good agreement with Exp. #4. However, the simulation seemed to slightly under-predict the range of crack lengths seen in the experiment. The results are summarised in Fig. 12.

4.1.3. Energy absorption and force displacement

The predicted evolution of the energy absorption for the inner chamfer crush tube is compared with the experimental measurements in Fig. 13. The time in the prediction is offset slightly to better match the moment when the impactor comes into contact with the tube. Initially, the absorbed energy rises more rapidly during the damage initiation phase until the drop in force at around $t = 1$ ms. Then, as the stable crushing force drops, the absorbed energy appears to grow at a slower pace before rebounding between $t = 3$ ms and $t = 5$ ms. In all experimental cases, the total absorbed energy was around 500 J, which corresponds to the energy of the impact and is reproduced in the simulation. Qualitatively, the trend of the predicted energy absorption history matches the simulations well and the curve appears to fall within the experimental scatter throughout the duration of the test.

Fig. 13 compares the predicted force–deflection curve with a representative experimental result (Exp. #4) to highlight the different attributes of the results. The prediction shows excellent correlation with

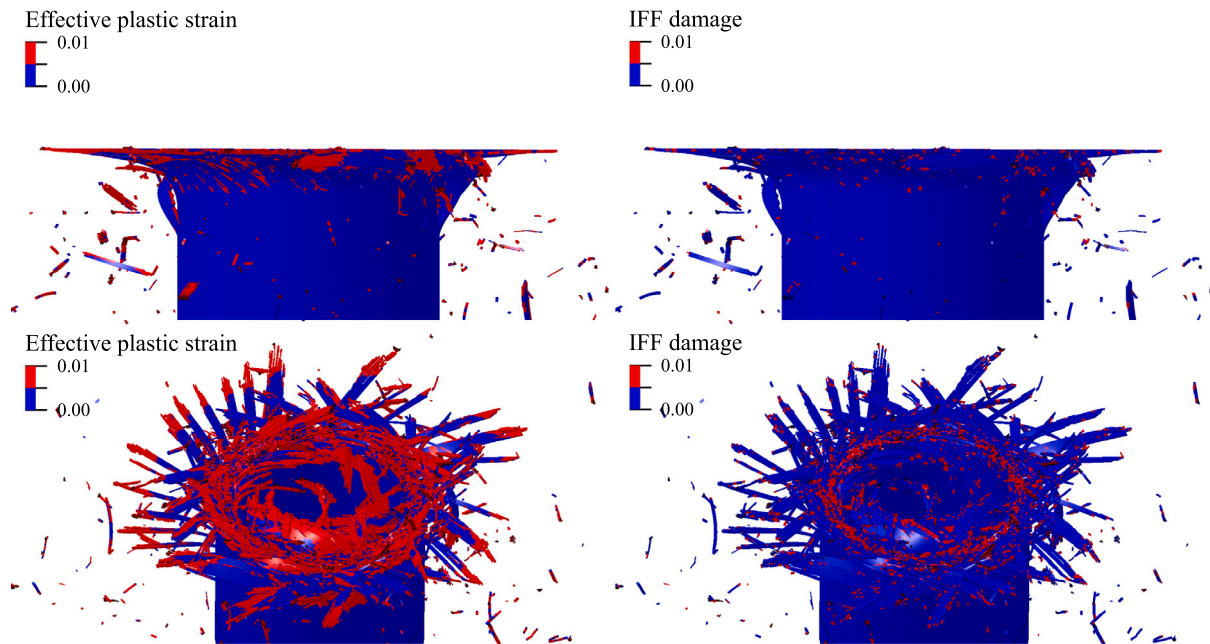


Fig. 10. Contours of effective plastic strain and IFF damage variables.

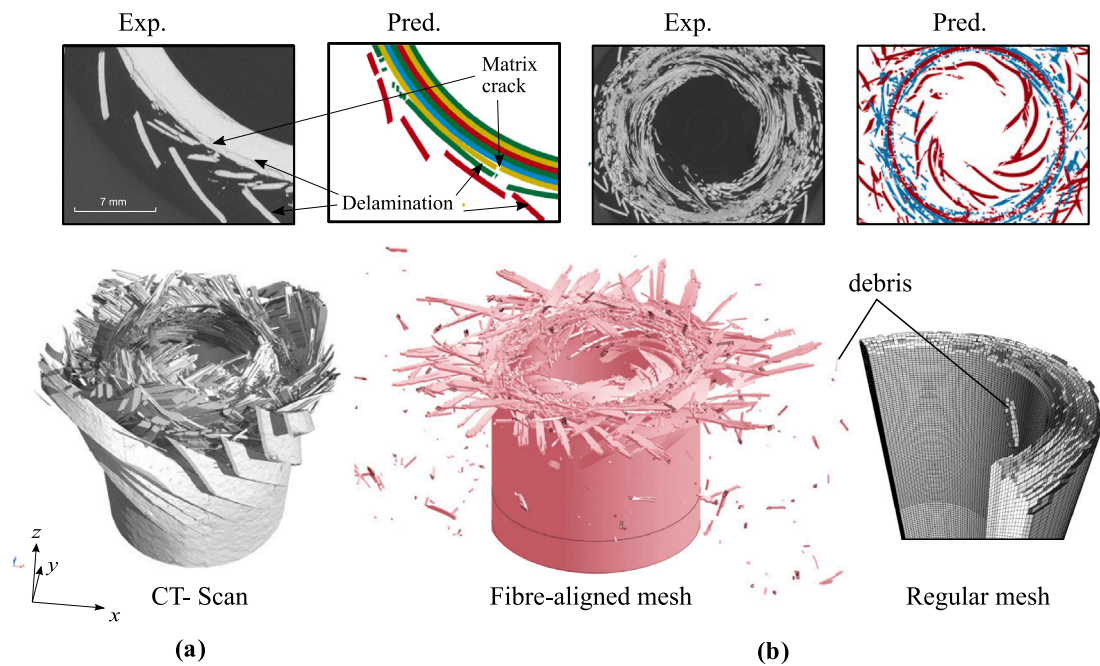


Fig. 11. (a) Macroscopic damage mechanisms after ultimate failure from the CT scan (15.3 mm crushing displacement) and simulation (15.5 mm crushing displacement). (b) Comparison of aligned mesh (left) and regular mesh (15.2 mm crushing displacement) (right).

the experimental results in terms of the overall shape and values for the peak force, crushing force, and total crushing displacement. In this example, three stages of the impact event are evident: (i) the damage initiation, (ii) crushing propagation, and (iii) impactor rebound. The damage initiation phase is followed by a small load drop before the force elevates further during the propagation phase. The model seems to be slightly stiffer than the experiment initially, which may be due to the slight compliance in the set-up as discussed in Section 2.3. However, the peak load is well predicted (Sim: 74 kN vs Exp. #4: 66 kN). The load drops prior to the peak seem to be attributed to the initiation of delamination. After 4 mm of displacement, the crash front has passed the chamfer and all plies have begun to delaminate and

widespread intra-ply matrix splits oriented along the fibre direction are present. During the propagation stage, the delamination and matrix cracks continue to grow. The matrix cracks seem to propagate more slowly than in the experiment, but achieve, on average, the same final crack length according to the CT based crack length measurements, which may be due to the stick-slip behaviour of the crack opening observed in the experiment that was not captured in the simulation. The lack of a debris wedge in the simulation, caused by element erosion, could also be a contributing factor. Energy is dissipated mainly through matrix cracking, interlaminar friction of disbonded plies and the continued growth of delaminations. The force increases slightly during the crushing stage until the drop weight rebounds. The predicted shape of

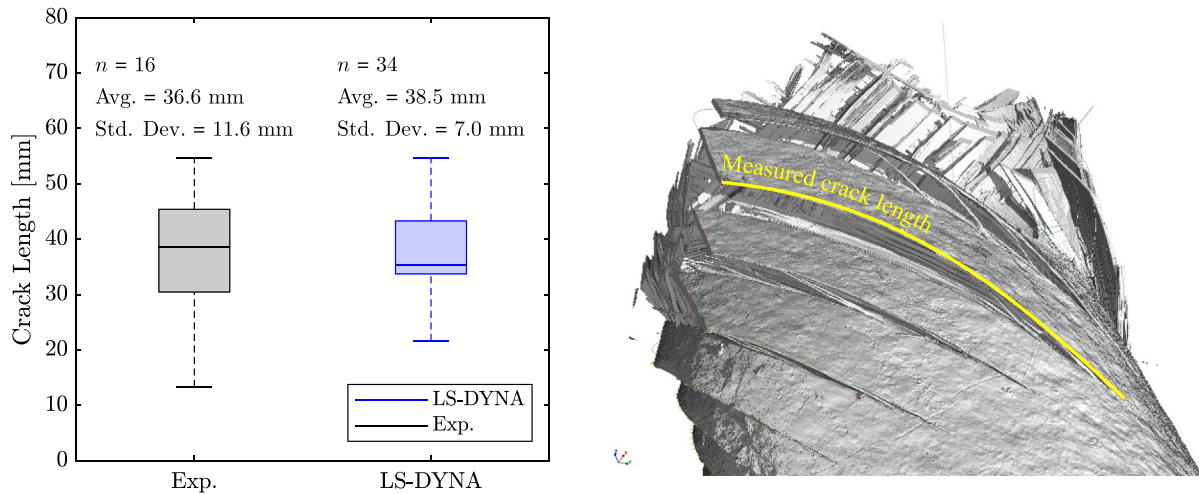


Fig. 12. Crack length measurements taken from the CT scan and simulation.

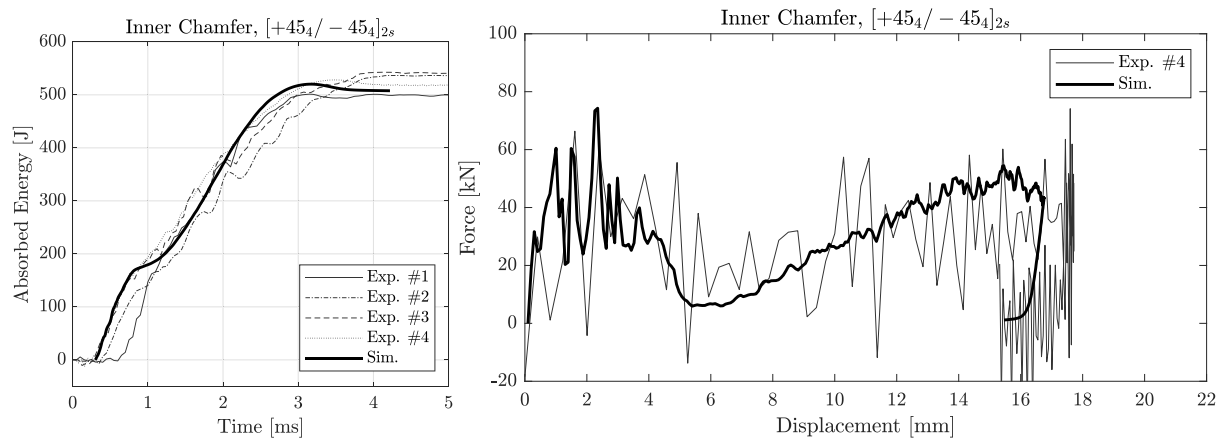


Fig. 13. Predicted energy absorption and force–displacement curve compared with experimental measurements for the inner chamfer.

the force–displacement curve during the rebound accurately matches the experimental curve. While the measured force seems to increase slightly during the propagation phase, the increase predicted by the simulation appears to be stronger than observed in the experiment. In this instance, the maximum displacement is slightly under-predicted, as the force at the end of the propagation phase seems to be slightly higher than the measured values. Still, the total crushing displacement in the simulation was 16.7 mm, which is within the experimental scatter (avg.: 18.4 mm, CV: 19.5%).

4.1.4. Energy evolution

The main energy dissipation mechanisms are compared in Fig. 14. The total energy remains nearly constant and the hourglass energy (HG) is sufficiently small ($\sim 10\%$) compared to the initial kinetic energy (KE) and internal energy (IE) of the CFRP. Slight variation in the total energy appears to be a numerical artefact associated with hourglass energy and non-physical element erosion. The kinetic energy of the drop weight is reduced as energy is dissipated and transferred into the CFRP. The drop weight rebounds slightly at the end of the impact event and regains a small amount of kinetic energy. The principal source of dissipation appears to occur in the interfaces between both the impactor–CFRP and CFRP–CFRP at interlaminar fracture surfaces including the internal energy, frictional dissipation and delamination energy. This highlights the importance of accurate inter- and intralaminar crack prediction for realistic behaviour at the interfaces. Furthermore, these results support the use of detailed, ply-by-ply modelling, where delamination, contact and friction between delaminated plies can be naturally modelled.

A sensitivity study in the following section was performed to illustrate/investigate how the accuracy of strength (rate-dependent), energy release rates, and crack propagation can strongly influence the accuracy of the overall prediction.

4.1.5. Parameter sensitivity

The influence of the model parameters is investigated in Fig. 15. The baseline case ($4\times$ delam. energy, contact friction, aligned mesh) from which all previous results were drawn is included as a reference. Reducing the delamination fracture energy to the reference values for a single interface reduces the crushing force during the propagation phase significantly. The crack length and delamination area are both increased. With $4\times$ delamination energy, but frictionless contact between delaminated plies, the crushing force is elevated, but not sufficiently to match the baseline results. These results suggest that the interplay between delamination and friction can have a strong influence on the energy dissipation. Deactivating rate-dependency in the plasticity model and failure criteria seemed to significantly reduce the peak force. The ply splits also increased in length and the crack density increased.

In addition, a case with a regular (non-aligned) mesh was included for comparison. The peak force and propagation force appear to be reasonable compared to the experiment/baseline case, but the reduction in force after the peak seems to be missing. The drop weight rebound is replicated in both the baseline model ($4\times$ delamination energy, friction, and aligned mesh) and the model with the regular mesh, but the other three cases with the aligned mesh failed to absorb/dissipate sufficient energy to stop/rebound the impactor. The evolution of the dissipated

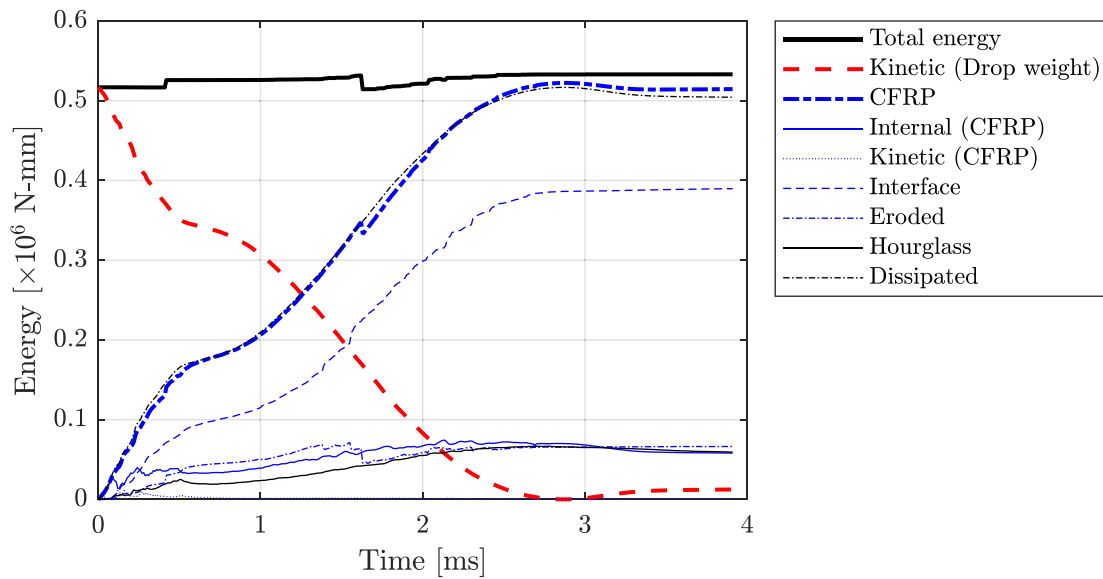


Fig. 14. Evolution of energy components from the crushing analysis.

energy is also shown for each case in Fig. 15. Initially, the energy dissipation from the model without rate effects is under-predicted. For $1\times$ delam. energy with friction and $4\times$ delam. energy without friction, the energy dissipation is well predicted through the initial peak force, but the rate of energy dissipation is reduced after approximately 5 mm of displacement and is under-predicted during the later stages of crushing. The energy dissipated from the regular mesh and baseline cases are similar throughout the analysis, but the shapes of the curves are different, with the regular mesh showing a nearly linear increase in energy dissipation for the duration of the simulation.

Although the force–displacement and energy dissipation produced by the regular mesh may be considered acceptable, the damage mechanisms do not match experimental observations. The elements at the crash front are rapidly damaged and eroded without producing the matrix cracks along the fibre-direction, also seen in Fig. 11(b). The incorrect prediction of the failure mechanisms means that the correlation of the drop weight response may be considered coincidental, rather than the product of sound physical modelling of the impact mechanics. However, reproducing the energy dissipation may be sufficient in certain applications. For the case studied here, a fibre-aligned mesh seems to be a critical aspect of the proposed modelling approach using the CDM technique, which allows both the fracture pattern and drop weight response to be reproduced.

4.2. Outer chamfer

To include an additional test case for further model validation, the outer chamfer geometry was analysed using the same procedure as before. To reduce the computational cost, the finite element size was selected to be 0.8×0.4 mm which was shown to yield excellent damage and energy absorption predictions with the inner chamfer (see Appendix B). The failure modes in the outer chamfer test are reasonably well predicted including the longitudinal ply splits, but the cracks do not propagate sufficiently ahead of the impactor as compared to the experiment.

4.2.1. Energy absorption and force–displacement

The predicted energy absorption history and force–displacement curves for the outer chamfer crush tube are compared with the experimental results in Fig. 16. In this case, looking at the absorbed energy curves, the change from damage initiation to stable crushing appears to be more gradual than in the inner chamfer case, which can be explained by the smaller difference between initiation and stable crushing

forces. Nevertheless, excellent agreement between the simulation and experiment was also obtained for this case, with only the peak force appearing to be slightly over predicted while the remainder of the force–displacement and energy dissipation curves being well predicted.

5. Conclusions

Experimental and numerical analysis of drop weight impact of $\pm 45^\circ$ CFRP circular crush tubes was performed in this work. Two trigger geometries were studied including both inner and outer 45° chamfers. The drop weight force, velocity, and displacement were measured using DIC with a high speed camera setup. *Post-mortem* CT scans revealed details of the crack patterns of the failed composite tubes. A numerical model was developed in LS-DYNA to simulated the composite crushing event of both chamfer geometries. Ply-by-ply modelling with a fibre-aligned mesh was utilised wherein the intralaminar damage was modelled with CDM and delamination was treated with cohesive (tiebreak) contact. Eight layers of elements were used to mesh the layup where one layer of elements accounted for one ply block (four plies clustered with the same orientation). The CDM model, previously implemented as an LS-DYNA UMAT [44], included a 3D plasticity model with rate- and pressure-dependence and damage.

Drop weight testing of the $\pm 45^\circ$ tubes resulted in significant delamination and intra-ply damage. The intralaminar matrix cracks were oriented along the fibre-direction and propagated well ahead of the drop weight. Delamination was observed both between ply blocks and lamina with the same orientation. The measured failure mechanisms were well captured by the progressive failure and damage analysis according to qualitative assessment and quantitative measurements of the crack length and density. Interlaminar friction between disbonded plies seemed to be one of the largest energy dissipation mechanisms in the numerical analysis. The simulation showed that the correct combination of delamination fracture energy and friction were required to produce an accurate prediction of the response. The input properties were physically relevant with minor tuning of the delamination fracture energy to overcome the limitations of the numerical discretisation. Excellent correlation of the energy absorption and force–displacement curves was also observed. The modelling strategy could be further improved by increasing the number of elements through the thickness to allow delamination within a ply block at added computational expense. In the present analysis, a fibre-aligned mesh was a critically important

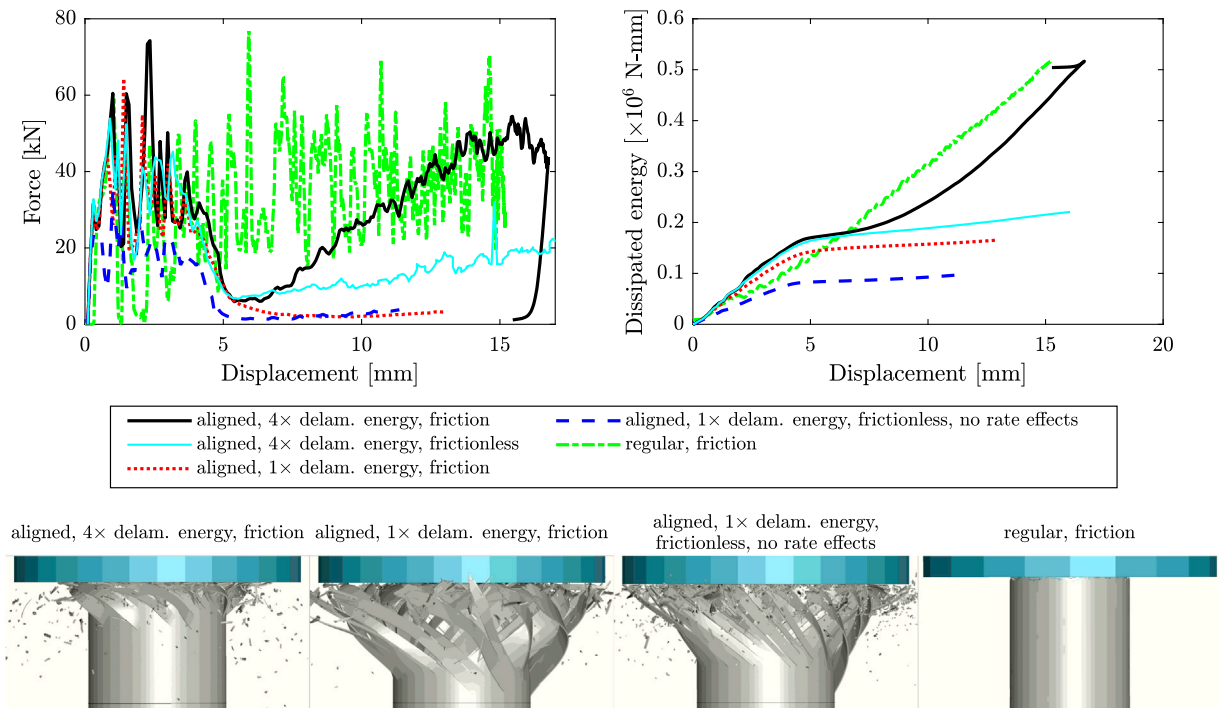


Fig. 15. Predicted force–displacement curves and damage at $t = 1$ ms using four different sets of parameters including delamination fracture energy, rate-dependent material model, and mesh alignment.

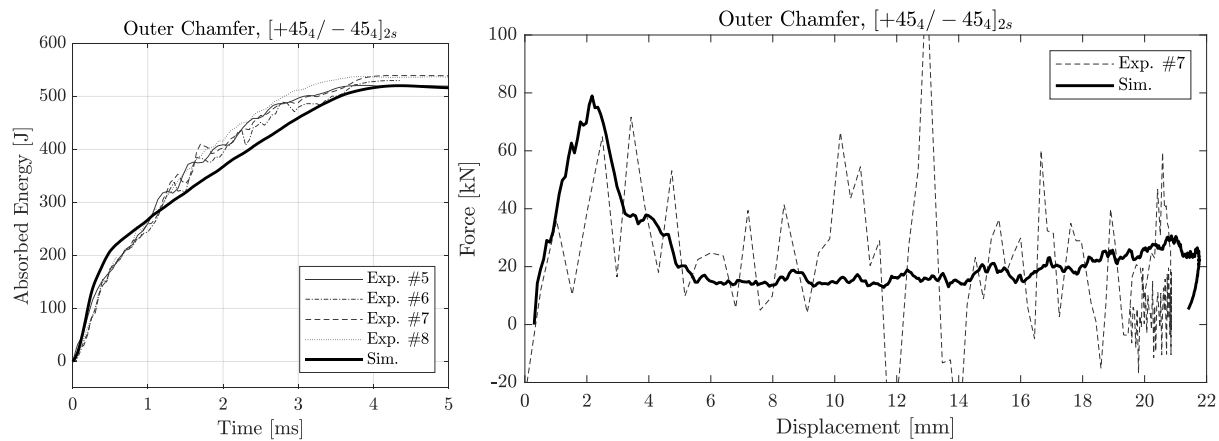


Fig. 16. Predicted energy absorption and force–displacement curve compared with experimental measurements for the outer chamfer.

modelling abstraction, which allowed the longitudinal ply splits to be obtained. A regular meshing scheme produced a reasonable prediction of the drop weight force–displacement, but the predicted damage mechanisms were non-physical wherein all of the elements under the drop weight were progressively eroded. The fibre-aligned mesh produced accurate damage predictions and drop weight behaviour (displacement, energy dissipation, and force–displacement curves).

Overall, the presented results demonstrate the maturity of current meso-scale modelling techniques for CFRP structures and components. As long as key deformation and failure mechanisms are included in the constitutive laws and an adequate mesh discretisation is used, high-fidelity numerical modelling of this kind is shown to be capable of capturing the experimental response to a high degree of accuracy. Along with other recent work in the literature (e.g., [21,23,36,40,42,63]), the accuracy of the results obtained here, not only in the specific energy absorption and force–displacement, but also the fracture morphology, permanent deformation, and residual structural integrity, shows the great potential of current high-fidelity modelling techniques

and represents continued progress towards virtual testing of CFRP structures and components.

CRediT authorship contribution statement

Drew E. Sommer: Conceptualization, Methodology, Formal analysis, Software, Validation, Visualization, Writing – original draft, Writing – review & editing. **D. Thomson:** Conceptualization, Methodology, Formal analysis, Software, Validation, Visualization, Writing – original draft, Writing – review & editing. **O. Falcó:** Conceptualization, Methodology, Formal analysis, Software, Validation, Visualization, Writing – review & editing. **G. Quino:** Methodology, Investigation, Writing – review & editing. **H. Cui:** Conceptualization, Methodology, Writing – review & editing. **N. Petrinic:** Project administration, Funding acquisition, Resources, Supervision.

Declaration of competing interest

Nik Petrinic reports financial support was provided by Mitsubishi Heavy Industries Ltd.

Data availability

The raw/processed data required to reproduce these findings cannot be shared at this time as the data also forms part of an ongoing study.

Acknowledgements

This work was supported by Mitsubishi Heavy Industries, Ltd. The authors would like to acknowledge the support from Rolls-Royce Plc. through the UTC for Solid Mechanics, University of Oxford. The authors would like to thank Holger Böhm, Moritz Kuhtz, Jonas Richter, and Andreas Hornig from the TU Dresden Institute of Lightweight Engineering and Polymer Technology (ILK) for performing the CT scan.

Appendix A. Constitutive modelling

In order to include strain-rate and pressure effects in the FEA predictions, the three-dimensional plasticity and damage model from [44, 57] was used to represent the behaviour of the CFRP in the presented simulations. The model is based on the idea that the same physical phenomena behind Puck's failure criterion may also explain the matrix-dominated nonlinear response observed in UD FRPs. The rate-dependent plasticity model was developed based on the same localisation plane concept used in Puck's IFF theory and, coupled with three-dimensional rate-dependent failure criteria in a continuum damage mechanics implementation, showed excellent agreement with off-axis loading experiments at quasi-static and dynamic loading rates for the IM7/8552 material used in the present study.

The yield criterion is based on finding the critical localisation plane that maximises the yield function below:

$$f = \bar{\sigma} [\sigma, \theta_{lp}] - \tau_y [\dot{\epsilon}_p] = \alpha \sigma_n + \sqrt{\tau_{n1}^2 + e \tau_{nt}^2} - \tau_y [\bar{\epsilon}] r [\dot{\epsilon}_p] = 0 \quad (\text{A.1})$$

Where σ_n , τ_{n1} , and τ_{nt} are the normal and shear tractions acting on the localisation plane, as illustrated by Fig. A.1. α and e are model parameters that define the shape of the yield envelope, and $\tau_y [\bar{\epsilon}]$ and $r [\dot{\epsilon}_p]$ represent the effects of strain hardening and strain-rate on the yield stress, respectively.

The localisation plane tractions can be obtained by rotating the material-oriented stress tensor around the fibre direction as follows:

$$\begin{Bmatrix} \sigma_1 \\ \sigma_n \\ \sigma_t \\ \tau_{n1} \\ \tau_{nt} \\ \tau_{1t} \end{Bmatrix} = \begin{bmatrix} 1 & 0 & 0 & 0 & 0 & 0 \\ 0 & c^2 & s^2 & 2sc & 0 & 0 \\ 0 & s^2 & c^2 & -2sc & 0 & 0 \\ 0 & 0 & 0 & c & 0 & s \\ 0 & -cs & -cs & 0 & c^2 - s^2 & 0 \\ 0 & 0 & 0 & -s & 0 & c \end{bmatrix} \begin{Bmatrix} \sigma_{11} \\ \sigma_{22} \\ \sigma_{33} \\ \tau_{12} \\ \tau_{23} \\ \tau_{13} \end{Bmatrix}, \quad (\text{A.2})$$

with $c = \cos[\theta]$ and $s = \sin[\theta]$

Isotropic strain hardening is modelled using a combined Voce function of the equivalent plastic strain, ϵ_p and the material parameters A , B_1 , B_2 , C_1 , and C_2 :

$$\tau_y [\bar{\epsilon}_p] = A + B_1 (1 - \exp[-C_1 \epsilon_p]) + B_2 (1 - \exp[-C_2 \epsilon_p]) \quad (\text{A.3})$$

The effect of strain-rate is then added by the following strain-rate scaling function with a single parameter, r_y :

$$r [\dot{\epsilon}] = 1 + \sqrt{r_y \dot{\epsilon}} \quad (\text{A.4})$$

Finally, non-associative plastic flow can be defined by choosing parameters α_g and e_g different than the parameters α and e from Eq. (A.1) in the flow rule below:

$$g[\bar{\sigma}] = \alpha_g \sigma_n + \sqrt{\tau_{n1}^2 + e_g \tau_{nt}^2} \quad (\text{A.5})$$

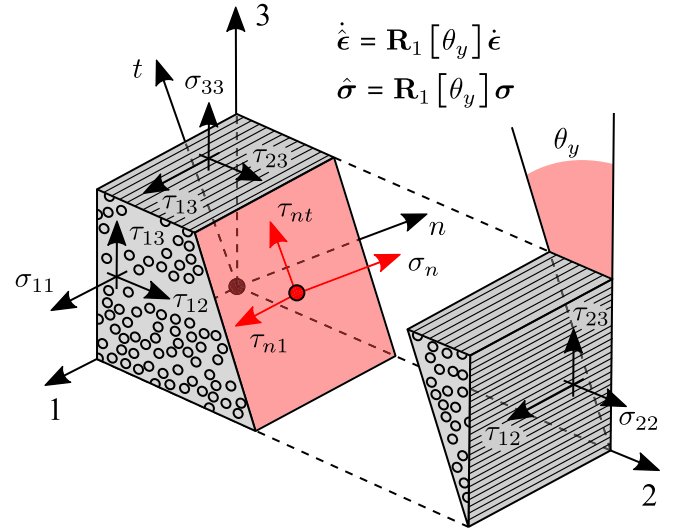


Fig. A.1. Schematic view of the plastic strain localisation plane, 1-t, defined by angle, θ_y , and the rotated tractions, σ_n , τ_{n1} , and τ_{nt} , that define the effective stress for both the yield and matrix failure criteria [44].

The above plasticity model is then coupled with the following failure criteria and damage model for each of the main failure modes.

IFF is predicted by Puck's criterion below:

$$f_{IFF} = \begin{cases} \sqrt{(1-p_t)^2 \left(\frac{\sigma_n}{Y_T}\right)^2 + \left(\frac{\tau_{n1}}{R_{n1}}\right)^2 + \left(\frac{\tau_{nt}}{R_{nt}}\right)^2} + p_t \frac{\sigma_n}{Y_T} \geq 1, & \text{for } \sigma_n \geq 0 \\ \sqrt{\left(p_c \frac{\sigma_n}{Y_C}\right)^2 + \left(\frac{\tau_{n1}}{R_{n1}}\right)^2 + \left(\frac{\tau_{nt}}{R_{nt}}\right)^2} + p_c \frac{\sigma_n}{Y_C} \geq 1, & \text{for } \sigma_n < 0 \end{cases} \quad (\text{A.6})$$

Where the frictional parameters p_t and p_c can be assumed rate-independent, and Y_T , R_{n1} , and R_{nt} can be assumed to scale with strain rate in the same way as the yield stress, following Eq. (A.4), as was shown in [53].

For fibre tension failure, a simple maximum stress criterion is used, as it can be assumed to not interact with off-axis stresses and is known to be rate-independent for CFRP:

$$f_{FT} = \frac{\sigma_{11}}{X_T} \geq 1 \quad (\text{A.7})$$

Finally, failure under fibre compression loading can be predicted by the kinking instability theory from Budiansky and Fleck [54]. Here, a rate-dependent formulation of this criterion is used, which was derived in [57] from the rate-dependent plasticity model described above.

$$f_{FC} [G_{12}, \sigma, \dot{\epsilon}_p] \geq 1 \quad (\text{A.8})$$

Following the onset of damage predicted by any of the three previous criteria, a continuum damage variable is defined below, which degrades the relevant stiffness properties for each failure mode. Damage accumulated during tensile loading is not allowed to degrade the stiffness during compression loading to simulate the crack closing effect.

$$D = \max \left\{ 0, \frac{\delta_C(\delta - \delta_0)}{\delta(\delta_C - \delta_0)} \right\} \quad (\text{A.9})$$

Where, $\delta = l_c \epsilon_{eff}$ is the effective crack opening displacement obtained as a function of the characteristic element length, l_c , and the effective driving strain, ϵ_{eff} , for the relevant failure mode. δ_0 is the effective displacement at the onset, and $\delta_C = 2G_C/\sigma_{eff}^C$ is the critical displacement at complete failure, with G_C being the associated fracture

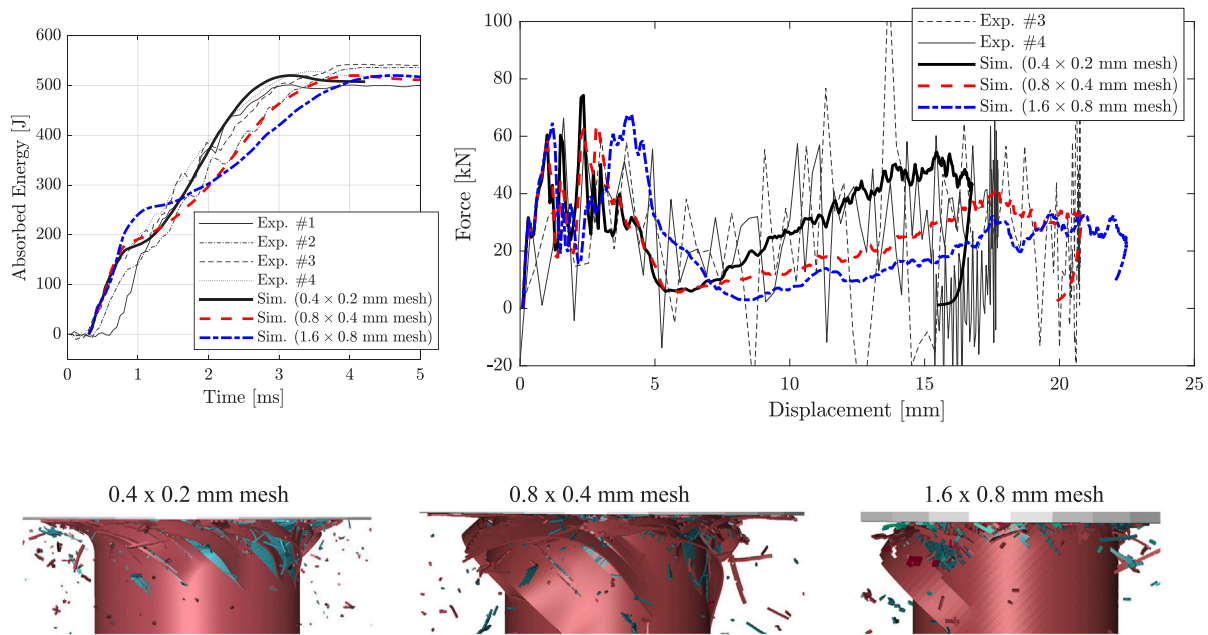


Fig. B.1. Mesh sensitivity for three different element sizes with a fixed aspect ratio of 2:1 (inner chamfer results) with damaged states shown 5 ms after impact.

energy and σ_{eff}^C the critical effective stress. For IFF, the mixed-mode fracture energy is obtained from the mode I and mode II energies as:

$$G_C = \frac{G_{IC}G_{IIC}(1 + \eta^2 \lambda)}{G_{IIC} + G_{IC}\eta^2 \lambda} \quad (A.10)$$

Where ρ is the mixed mode ratio, and $\lambda = E_2/G_{12}$ is the stiffness ratio between opening and shear moduli. Within the CDM framework, the energy released over the total fracture area must be greater than the internal energy of the element. In practical terms this puts a limit on the maximum element size, which can be expressed as:

$$G_C \geq \frac{1}{2} X_0 \delta_0 = \frac{1}{2} X_0 \frac{X_0}{E} l_c \quad (A.11)$$

This defines the maximum characteristic element length as a function of the fracture toughness, stress, and strain at the onset of failure, rewritten above in terms of the strength, X_0 , and stiffness, E , associated with the relevant failure mode. In the case of rate-dependent strength properties, as used in the present study, the maximum element size will decrease as the strain-rate increases.

Finally, for all three failure modes, element erosion is activated when any of the damage variables reaches 1, indicating complete damage. In addition, LS-DYNA solver controls were used to delete any elements with negative volumes due to excessive distortion. However, since this can compromise the stability of the solution, additional geometry-based element erosion was included to remove heavily distorted elements that may have escaped the damage-based criteria:

$$\frac{DR_n}{DR_0} \geq DDL \quad (A.12)$$

Where DDL is the prescribed the upper limit for the element diagonal distortion before it will be deleted, and DR_n and DR_0 are a measure of the element diagonal ratio at the current, n th, time increment and at the start of the simulation, respectively.

$$DR_n = \frac{\max(p_{17}, p_{28}, p_{35}, p_{46})}{\min(p_{17}, p_{28}, p_{35}, p_{46})} \quad (A.13)$$

Where p_{ij} are the element diagonals for an 8-node hexahedral element, computed from the nodal coordinates of nodes 1 to 7 at the n th time increment.

The calibrated model parameters for IM7/8552 obtained from [44, 57] are given in Table 2.

Appendix B. Mesh sensitivity

The mesh sensitivity of the inner chamfer crushing analysis is shown in Fig. B.1 for three element sizes. Despite the use of mesh regularisation, some mesh dependence is to be expected with CDM modelling [64]. The element aspect ratio was fixed at 2:1 (length \times width) and the in-plane dimensions were scaled by a factor of two or four relative to the finest mesh density (0.4×0.2 mm). The number of elements through the thickness was maintained at eight. To satisfy the energy dissipation requirements, the element size should be limited according to the material properties and characteristic length, which can lead the fracture energy to be artificially increased for larger elements. Further information about mesh objectivity in damage modelling can be found in [65–68]. Additionally, the mesh size influences quality of the discretisation of the circular cross-section of the tube. The predicted energy absorption and force–displacement curves are within the experimental scatter for all mesh densities although some differences can be observed. With the both the smallest and intermediate element sizes, the failure modes are well predicted. However, for the coarsest mesh, excessive element erosion is observed under the drop-weight and the cracks are poorly predicted. In addition, the coarse mesh showed more significant differences in the predicted behaviour, with a longer predicted damage initiation phase and greater energy dissipation during the stable crushing phase, which may be attributed to the element size issues mentioned above. Compared to the finest mesh (which required 94 h computation time), the intermediate and coarse meshes were much more efficient, requiring approximately 10 h and 2 h computation time, respectively. These results suggest that the mesh sensitivity is modest and within the anticipated range for this type of damage modelling.

Appendix C. Supplementary data

Supplementary material related to this article can be found online at <https://doi.org/10.1016/j.compositesa.2022.107033>.

References

- [1] Schmueser DW, Wickliffe LE. Impact energy absorption of continuous fiber composite tubes. *J Eng Mater Technol* 1987;109(1):72–7.
- [2] Hull D. A unified approach to progressive crushing of fibre-reinforced composite tubes. *Compos Sci Technol* 1991;40(4):377–421.
- [3] Farley GL, Jones RM. Crushing characteristics of continuous fiber-reinforced composite tubes. *J Compos Mater* 1992;26(1):37–50.
- [4] Huang J, Wang X. Numerical and experimental investigations on the axial crushing response of composite tubes. *Compos Struct* 2009;91(2):222–8.
- [5] Xiao X, Botkin ME, Johnson NL. Axial crush simulation of braided carbon tubes using MAT58 in LS-DYNA. *Thin-Walled Struct* 2009;47(6–7):740–9.
- [6] McGregor C, Vaziri R, Xiao X. Finite element modelling of the progressive crushing of braided composite tubes under axial impact. *Int J Impact Eng* 2010;37(6):662–72.
- [7] Chiu LN, Falzon BG, Ruan D, Xu S, Thomson RS, Chen B, et al. Crush responses of composite cylinder under quasi-static and dynamic loading. *Compos Struct* 2015;131:90–8.
- [8] Luo H, Yan Y, Meng X, Jin C. Progressive failure analysis and energy-absorbing experiment of composite tubes under axial dynamic impact. *Composites B* 2016;87:1–11.
- [9] Shor O, Vaziri R. Application of the local cohesive zone method to numerical simulation of composite structures under impact loading. *Int J Impact Eng* 2017;104:127–49.
- [10] McGregor C, Zobeiry N, Vaziri R, Poursartip A, Xiao X. Calibration and validation of a continuum damage mechanics model in aid of axial crush simulation of braided composite tubes. *Composites A* 2017;95:208–19.
- [11] Nishi M, Saito K, Ren B. Discrete FE modeling to simulate micro-fracture modes in progressive crushing of fiber reinforced composite tubes. In: *ECCM 2018-18th eur. conf. compos. mater.*
- [12] Cherniaev A, Butcher C, Montesano J. Predicting the axial crush response of CFRP tubes using three damage-based constitutive models. *Thin-Walled Struct* 2018;129:349–64.
- [13] Zhu G, Sun G, Li G, Cheng A, Li Q. Modeling for CFRP structures subjected to quasi-static crushing. *Compos Struct* 2018;184:41–55.
- [14] David M, Johnson AF, Voggenreiter H. Analysis of crushing response of composite crashworthy structures. *Appl Compos Mater* 2013;20(5):773–87.
- [15] Bru T, Waldenström P, Gutkin R, Olsson R, Vyas GM. Development of a test method for evaluating the crushing behaviour of unidirectional laminates. *J Compos Mater* 2017;51(29):4041–51.
- [16] Waimer M, Siemann MH, Feser T. Simulation of CFRP components subjected to dynamic crash loads. *Int J Impact Eng* 2017;101:115–31.
- [17] Liu Z, Xia Y. Development of a numerical material model for axial crushing mechanical characterization of woven CFRP composites. *Compos Struct* 2019;230:111531.
- [18] Dalli D, Varandas LF, Catalanotti G, Foster S, Falzon BG. Assessing the current modelling approach for predicting the crashworthiness of formula one composite structures. *Composites B* 2020;201:108242.
- [19] Tan W, Falzon BG, Price M. Predicting the crushing behaviour of composite material using high-fidelity finite element modelling. *Int J Crashworthiness* 2015;20(1):60–77.
- [20] Chiu LN, Falzon BG, Boman R, Chen B, Yan W. Finite element modelling of composite structures under crushing load. *Compos Struct* 2015;131:215–28.
- [21] Tan W, Falzon BG. Modelling the crush behaviour of thermoplastic composites. *Compos Sci Technol* 2016;134:57–71.
- [22] Tan W, Falzon BG, Price M, Liu H. The role of material characterisation in the crush modelling of thermoplastic composite structures. *Compos Struct* 2016;153:914–27.
- [23] Chiu LNS, Falzon BG, Chen B, Yan W. Validation of a 3D damage model for predicting the response of composite structures under crushing loads. *Compos Struct* 2016;147:65–73.
- [24] Siromani D, Awerbuch J, Tan T-M. Finite element modeling of the crushing behavior of thin-walled CFRP tubes under axial compression. *Composites B* 2014;64:50–8.
- [25] Reuter C, Sauerland K-H, Tröster T. Experimental and numerical crushing analysis of circular CFRP tubes under axial impact loading. *Compos Struct* 2017;174:33–44.
- [26] Grotto F, Rivallant S, Bouvet C. Development of a 3D finite element model at mesoscale for the crushing of unidirectional composites: Application to plates crushing. *Compos Struct* 2022;287:115346.
- [27] Forghani A. A non-local approach to simulation of damage in composite structures [Ph.D. thesis], University of British Columbia; 2011.
- [28] Forghani A, Zobeiry N, Poursartip A, Vaziri R. A structural modelling framework for prediction of damage development and failure of composite laminates. *J Compos Mater* 2013;47(20–21):2553–73.
- [29] Zobeiry N, Forghani A, McGregor C, McClelland S, Vaziri R, Poursartip A. Effective calibration and validation of a nonlocal continuum damage model for laminated composites. *Compos Struct* 2017;173:188–95.
- [30] Reiner J, Feser T, Waimer M, Poursartip A, Voggenreiter H, Vaziri R. Axial crush simulation of composites using continuum damage mechanics: FE software and material model independent considerations. *Composites B* 2021;225:109284.
- [31] Feraboli P, Wade B, Deleo F, Rassaian M, Higgins M, Byar A. LS-DYNA MAT54 modeling of the axial crushing of a composite tape sinusoidal specimen. *Composites A* 2011;42(11):1809–25.
- [32] Hoffarth C, Rajan SD, Goldberg RK, Revilock D, Carney KS, DuBois P, et al. Implementation and validation of a three-dimensional plasticity-based deformation model for orthotropic composites. *Composites A* 2016;91:336–50.
- [33] Goldberg RK, Carney KS, DuBois P, Hoffarth C, Harrington J, Rajan S, et al. Development of an orthotropic elasto-plastic generalized composite material model suitable for impact problems. *J Aerosp Eng* 2016;29(4):04015083.
- [34] Hoffarth C, Khaled B, Shyamsunder L, Rajan S, Goldberg R, Carney KS, et al. Verification and validation of a three-dimensional orthotropic plasticity constitutive model using a unidirectional composite. *Fibers* 2017;5(1):12.
- [35] Khaled BM, Shyamsunder L, Holt N, Hoover CG, Rajan SD, Blankenhorn G. Enhancing the predictive capabilities of a composite plasticity model using cohesive zone modeling. *Composites A* 2019;121:1–17.
- [36] Justusson B, Molitor M, Schaefer J, Liguore SL, Ranatunga V, Pigazzini M. The use of LS-DYNA MAT299 for accurate prediction of impact damage in composite structures. In: *AIAA scitech 2021 forum*. 2021. p. 1624.
- [37] Leone Jr FA. Deformation gradient tensor decomposition for representing matrix cracks in fiber-reinforced materials. *Composites A* 2015;76:334–41.
- [38] Achard V, Bouvet C, Castanié B, Chirol C. Discrete ply modelling of open hole tensile tests. *Compos Struct* 2014;113:369–81.
- [39] Lopes C, Sádaba S, González C, Llorca J, Camanho P. Physically-sound simulation of low-velocity impact on fiber reinforced laminates. *Int J Impact Eng* 2016;92:3–17.
- [40] Falcó O, Ávila RL, Tijs B, Lopes CS. Modelling and simulation methodology for unidirectional composite laminates in a Virtual Test Lab framework. *Compos Struct* 2018;190:137–59.
- [41] Joseph APK, Davidson P, Waas AM. Open hole and filled hole progressive damage and failure analysis of composite laminates with a countersunk hole. *Compos Struct* 2018;203:523–38.
- [42] Lopes CS, Gómez DG, Falcó O, Tijs BH. Stochastic virtual testing laboratory for unidirectional composite coupons: From conventional to dispersed-ply laminates. In: *Multi-scale continuum mechanics modelling of fibre-reinforced polymer composites*. Elsevier; 2021, p. 579–607.
- [43] Sommer DE, Thomson D, Falcó O, Quino G, Cui H, Petrinic N. High-fidelity damage modelling of CFRP laminates for impact and crashworthiness applications—dynamic tube crushing simulations. In: *EPJ web of conferences*. 250, EDP Sciences; 2021, p. 02014.
- [44] Thomson DM, Erice B, Cui H, Hoffmann J, Wiegand J, Petrinic N. A puck-based localisation plane theory for rate- and pressure-dependent constitutive modelling of unidirectional fibre-reinforced polymers. *Compos Struct* 2018;184:299–305.
- [45] Böhm R, Stiller J, Behnisch T, Zscheyge M, Protz R, Radloff S, et al. A quantitative comparison of the capabilities of in situ computed tomography and conventional computed tomography for damage analysis of composites. *Compos Sci Technol* 2015;110:62–8.
- [46] Liu X, Belkassam B, Jonet A, Lecompte D, Van Hemelrijck D, Pintelon R, et al. Experimental investigation of energy absorption behaviour of circular carbon/epoxy composite tubes under quasi-static and dynamic crush loading. *Compos Struct* 2019;227:111266.
- [47] Nak-Ho S, Suh NP. Effect of fiber orientation on friction and wear of fiber reinforced polymeric composites. *Wear* 1979;53(1):129–41.
- [48] Li Y, Zhang W, Yang Z-w, Zhang J-y, Tao S-j. Low-velocity impact damage characterization of carbon fiber reinforced polymer (CFRP) using infrared thermography. *Infrared Phys Technol* 2016;76:91–102.
- [49] Sheikh-Ahmad J, Almaskari F, El-Hofy M. Characterization of the cutting forces and friction behavior in machining UD-CFRP using slot milling test. *Int J Adv Manuf Technol* 2021;112(11):3471–83.
- [50] Tripathy BS, Furey MJ. Tribological behavior of unidirectional graphite-epoxy and carbon-PEEK composites. *Wear* 1993;162:385–96.
- [51] Cui H, Thomson D, Pellegrino A, Wiegand J, Petrinic N. Effect of strain rate and fibre rotation on the in-plane shear response of $\pm 45^\circ$ laminates in tension and compression tests. *Compos Sci Technol* 2016;135:106–15.
- [52] Koerber H, Xavier J, Camanho PP. High strain rate characterisation of unidirectional carbon-epoxy IM7-8552 in transverse compression and in-plane shear using digital image correlation. *Mech Mater* 2010;42(11):1004–19.
- [53] Thomson DM, Cui H, Erice B, Hoffmann J, Wiegand J, Petrinic N. Experimental and numerical study of strain-rate effects on the IFF fracture angle using a new efficient implementation of Puck's criterion. *Compos Struct* 2017;181:325–35.
- [54] Budiansky B, Fleck NA. Compressive failure of fibre composites. *J Mech Phys Solids* 1993;41(1):183–211.
- [55] Pinho ST, Iannucci L, Robinson P. Physically-based failure models and criteria for laminated fibre-reinforced composites with emphasis on fibre kinking: Part I: Development. *Composites A* 2006;37(1):63–73.
- [56] Cui H, Thomson D, Eskandari S, Petrinic N. A critical study on impact damage simulation of IM7/8552 composite laminate plate. *Int J Impact Eng* 2019;127:100–9.

- [57] Thomson D, Quino G, Cui H, Pellegrino A, Erice B, Petrinic N. Strain-rate and off-axis loading effects on the fibre compression strength of CFRP laminates: Experiments and constitutive modelling. *Compos Sci Technol* 2020;195:108210.
- [58] Lemmen PPM, Meijer GJ. Failure prediction tool theory and user manual. TNO Report, 2001.
- [59] Xu X, Wisnom MR, Li X, Hallett SR. A numerical investigation into size effects in centre-notched quasi-isotropic carbon/epoxy laminates. *Compos Sci Technol* 2015;111:32–9.
- [60] Laš V, Zemčík R. Progressive damage of unidirectional composite panels. *J Compos Mater* 2008;42(1):25–44.
- [61] Millen SLJ, Ullah Z, Falzon BG. On the importance of finite element mesh alignment along the fibre direction for modelling damage in fibre-reinforced polymer composite laminates. *Compos Struct* 2021;278:114694.
- [62] Leone FA, Justusson BP. Effects of characteristic element length on fracture energy dissipation in continuum damage mechanics models. *J Compos Mater* 2021;00219983211023790.
- [63] LLorca J, González C, Molina-Aldareguía JM, Segurado J, Seltzer R, Sket F, et al. Multiscale modeling of composite materials: A roadmap towards virtual testing. *Adv Mater* 2011;23(44):5130–47.
- [64] Falcó O, Lopes CS, Sommer DE, Thomson D, Ávila R, Tijs B. Experimental analysis and simulation of low-velocity impact damage of composite laminates. *Compos Struct* 2022;287:115278.
- [65] Bažant ZP, Oh BH. Crack band theory for fracture of concrete. *Mater Struct* 1983;16(3):155–77.
- [66] Pinho ST, Iannucci L, Robinson P. Physically based failure models and criteria for laminated fibre-reinforced composites with emphasis on fibre kinking. Part II: Fe implementation. *Composites A* 2006;37(5):766–77.
- [67] Tan W, Falzon BG, Chiu LNS, Price M. Predicting low velocity impact damage and compression-after-impact (CAI) behaviour of composite laminates. *Composites A* 2015;71:212–26.
- [68] Rajaneesh A, Ponhot J-P, Bruyneel M. High velocity impact response of composite laminates using modified meso-scale damage models. *Int J Impact Eng* 2021;147:103701.